International Design Study for the
Neutrino Factory

IDS-NF-???
Other preprint and report numbers

Reference Design Report

The IDS-NF collaboration

Draft 0

July 8, 2013

S. Choubey, R. Gandhi, S. Goswami
Harish-Chandra Research Institute, Chhatnag Road, Jhunsi, Allahabad, 211019, India
J.S. Berg, R. Fernow, J.C. Gallardo, R. Gupta, H. Kirk, N. Simos, N. Souchlas
Brookhaven National Lab, P.O. Box 5000, Upton, NY 11973-5000, USA
M. Ellis[1], P. Kyberd
Brunel University West London, Uxbridge, Middlesex UB8 3PH, UK
E. Benedetto, E. Fernandez-Martinez, I. Efthymiopoulos, R. Garoby, S. Gilardoni, M. Martini, G. Prior
European Organization for Nuclear Research, CERN CH-1211, Geneva 23, Switzerland
D. Indumathi, N. Sinha
The Institute of Mathematical Sciences, IV Cross Road, CIT Campus, Taramani, Chennai 600 113, Tamil Nadu, India
P. Ballett, S. Pascoli
Institute for Particle Physics Phenomenology, Department of Physics, University of Durham, Science Laboratories, South Rd, Durham, DH1 3LE, UK
A. Bross, S. Geer, C. Johnstone, J. Kopp, N. Mokhov, J. Morfin, D. Neuffer, S. Parke, M. Popovic, J. Strait, S. Striganov
Fermilab, P.O. Box 500, Batavia, IL 60510-5011, USA
A. Blondel, F. Dufour
University de Geneve, 24, Quai Ernest-Ansermet, 1211 Geneva 4, Suisse
A. Laing, F.J.P. Soler
School of Physics and Astronomy, Kelvin Building, University of Glasgow, Glasgow G12 8QQ, Scotland, UK
M. Lindner, T. Schwetz
Max Planck Institut für Kernphysik, PO Box 103980, 69029 Heidelberg, Germany
A. Alekou, M. Apollonio, M. Aslaninejad, C. Bontoiu, P. Dornan, R. Eccleston, A. Kurup, K. Long, J. Pasternak, J. Pozimski
Physics Department, Blackett Laboratory, Imperial College London, Exhibition Road, London, SW7 2AZ, UK
A. Bogacz, V. Morozov, Y. Roblin
Thomas Jefferson National Laboratory, 12000 Jefferson Avenue, Newport News, VA 23606, USA
S. Bhattacharya, D. Majumdar
Saha Institute of Nuclear Physics, Sector-I, Block-AF, Bidhannagar, Kolkata 700064, India
Y. Mori, T. Planche[2]
Kyoto University, Research Reactor Institute, 2,Asashiro-Nishi, Kumatori-cho, Sennan-gun, Osaka 590-0494 Japan
M. Zisman
Lawrence Berkeley National Laboratory, 1 Cyclotron Road, Berkeley, CA 94720, USA
D. Cline, D. Stratakis, X. Ding
Department of Physics and Astronomy, University of California, Los Angeles, CA 90095, USA
P. Coloma, A. Donini[3], B. Gavela, J. Lopez Pavon, M. Maltoni
Universidad Autonoma de Madrid and Instituto de Fisica Teorica, UAM/CSIC, Cantoblanco, E-28049, Madrid, Spain;
C. Bromberg
Michigan State University, 150 Administration Building, East Lansing, Michigan 48824, USA

---

[1] Now at Westpac Institutional Bank, Sydney, NSW, Australia

[2] Now at TRIUMF, 4004 Wesbrook Mall, Vancouver, B.C., V6T 2A3, Canada

[3] Also at Universidad de Valencia and Instituto de Fisica Corpuscular, UV/CSIC, Apart. 22085, E-46071, Valencia, Spain

M. Bonesini
Sezione INFN Milano Bicocca, Dipartimento di Fisica G. Occhialini, Piazza Scienza 3, 20126 Milano, Italy
T. Hart
The University of Mississippi, Department of Physics and Astronomy, 108 Lewis Hall, PO Box 1848, Oxford, Mississippi 38677-1848, USA
Y. Kudenko
Institute for Nuclear Research of Russian Academy of Sciences, 7a, 60th October Anniversary prospect, Moscow 117312, Russia
N. Mondal
Tata Institute of Fundamental Research, School of Natural Sciences, Homi Bhabha Rd., Mumbai 400005, India
S. Antusch, M. Blennow, T. Ota
Max Planck Institut für Physik, Werner Heisenberg Institut für Physik, Fohringer Ring 6, D-80805 Munich, Germany
R.J. Abrams, C.M. Ankenbrandt, K.B. Beard, M.A.C. Cummings, G. Flanagan, R.P. Johnson, T.J. Roberts, C.Y. Yoshikawa
Muons Inc., 552 N. Batavia Avenue, Batavia, IL 60510, USA
P. Migliozzi, V. Palladino
Universita di Napoli Federico II, Dipartimento di Scienze Fisiche, Complesso Universitario di Monte S. Angelo, via Cintia, I-80126 Napoli, Italy
A. de Gouvea
Northwestern University, Dept. of Physics and Astronomy, 2145 Sheridan Road, Evanston, Illinois 60208-3112 USA
P. Snopok
Illinois Institute of Technology, 3101 S Dearborn St, Chicago, IL 60616, USA
V.B. Graves
Oak Ridge National Laboratory, P.O. Box 2008, Oak Ridge, TN 37831, USA
Y. Kuno
Osaka University, Graduate School, School of Science, 1-1 Machikaneyama-cho, Toyonaka, Osaka 560-0043, Japan
J. Peltoniemi
Puulinnankatu 12 F 50, FI-90570 Oulu, Finland
V. Blackmore, J. Cobb, C. Tunnell, H. Witte
Particle Physics Department, The Denys Wilkinson Building, Keble Road, Oxford, OX1 3RH, UK
M. Mezzetto, S. Rigolin
Dipartimento di Fisica, Universita di Padova and INFN Padova, Via Marzolo 8, I-35131, Padova, Italy
K.T. McDonald
Princeton University, Princeton, NJ, 08544, USA
L. Coney, G. Hanson
Department of Physics and Astronomy, University of California, Riverside, CA 92521, USA
L. Tortora
Sezione INFN Roma Tre, Dipartimento di Fisica E. Amaldi, Via della Vasca Navale 84, 00146 Roma, Italy
C. Andreopoulos, J.R.J. Bennett, S. Brooks, O. Caretta, T. Davenne, C. Densham, R. Edgecock[4], D. Kelliher, P. Loveridge, A. McFarland, S. Machida, C. Prior, G. Rees, C. Rogers, J.W.G. Thomason
STFC Rutherford Appleton Laboratory, Chilton, Didcot, Oxfordshire, OX11 0QX, UK

---

[4] also at University of Huddersfield, Queensgate, Huddersfield, HD1 3DH, UK

C. Booth, G. Skoro
University of Sheffield, Dept. of Physics and Astronomy, Hicks Bldg., Sheffield S3 7RH, UK
Y. Karadzhov[5], R. Matev, R. Tsenov
Department of Atomic Physics, St. Kliment Ohridski University of Sofia, 5 James Bourchier Boulevard, BG-1164 Sofia, Bulgaria
R. Samulyak
Physics and Astronomy Department, Stony Brook University, Stony Brook, NY 11794-3800, USA
S.R. Mishra, R. Petti
Department of Physics and Astronomy, University of South Carolina, Columbia SC 29208, USA
M. Dracos
IPHC, Université de Strasbourg, CNRS/IN2P3, F-67037 Strasbourg, France
O. Yasuda
Department of Physics, Toyko Metropolitan University, 1-1 Minami-Osawa, Hachioji-shi, Toyko, Japan 192-0397
S.K. Agarwalla, A. Cervera-Villanueva, J.J. Gomez-Cadenas, P. Hernandez, T. Li, J. Martin-Albo
Instituto de Fisica Corpuscular (IFIC), Centro Mixto CSIC-UVEG, Edificio Investigacion Paterna, Apartado 22085, 46071 Valencia, Spain
P. Huber
Virginia Polytechnic Inst. and State Univ., Physics Dept., Blacksburg, VA 24061-0435
J. Back, G. Barker, P. Harrison
Department of Physics, University of Warwick, Coventry, CV4 7AL, UK
D. Meloni, J. Tang, W. Winter
Fakultät für Physik und Astronomie, Am Hubland, 97074 Würzburg, Germany

---

[5] Now at the University of Geneva, Geneva, Switzerland

Foreword

This is what we said in the IDR ...
The International Design Study for the Neutrino Factory (the IDS-NF) [1] was established by the community at the ninth “International Workshop on Neutrino Factories, super-beams, and beta-beams” which was held in Okayama in August 2007 [2]. The IDS-NF mandate is to deliver the Reference Design Report (RDR) for the facility on the timescale of 2012/13 [3]. The RDR is conceived as the document upon which requests for the resources to carry out the first phase of the Neutrino Factory project can be made. The RDR will include: the physics performance of the Neutrino Factory and the specification of each of the accelerator, diagnostic, and detector systems; an estimate of the cost of the facility; and an estimate of the schedule for its implementation. The RDR will also include a discussion of the remaining technical risks and an appropriate risk-mitigation plan.

Executive summary

Lead author: KL

Contents

1 Introduction

The properties of the neutrino make it a unique tool for the study of fundamental physics. Alone among the fundamental fermions, the neutrino has no electric charge; it interacts solely via the weak force. The mass of the neutrino is tiny compared to the mass of all the other fundamental fermions. With no electric charge, it is possible that the neutrino and its antiparticle are the same, i.e. the neutrino is a "Majorana" fermion. The observation of the decay of a nucleus to two electrons or two positrons without any accompanying neutrinos (neutrinoless double-beta decay) would imply that the neutrino is Majorana in nature. In the Universe of today, the abundance of neutrinos is second only to that of photons. The weakness of the neutrino interaction with matter allows the neutrino to travel great distances through the Universe, thereby playing an important role in the evolution of the cosmos. Historically, the study of neutrino interactions has been seminal in the development of the Standard Model (SM) of particle physics. The recent discovery that the flavour of a neutrino changes as it propagates through space and time, a phenomenon known as "neutrino oscillations", provides the germ for the development of a deeper understanding of the physics of fundamental particles and the impact of the neutrino on the evolution of the Universe. However, the fact that neutrinos interact only weakly with matter means that novel techniques must be developed to provide data sets of the quality and size required to study the details of neutrino oscillation. The Neutrino Factory described in this report employs a novel accelerator complex to generate high-energy neutrino beams of uniquely well-defined flux and flavour composition from the decay of muons confined within a storage ring.

Neutrino oscillations may be described as arising from the "beating" of the phase of neutrino-mass eigenstates in the propagation of a neutrino produced as an eigenstate of flavour. The three flavour eigenstates, ν_e, ν_μ, and ν_τ may be written as linear superpositions of the mass eigenstates, ν_1, ν_2, and ν_3. To describe neutrino oscillations, the matrix by which the neutrino mass basis is rotated into the neutrino flavour basis is usually parameterised in terms of three mixing angles (θ_{12}, θ_{23}, and θ_{13}) and one phase parameter (δ) [4–7]. The measured values of the neutrino-mixing angles are large, much larger than those observed in the quark sector. If δ is non-zero, the symmetry between the properties of matter and antimatter will be broken via the neutrino mixing matrix. Measurements of neutrino oscillations are not sensitive to the neutrino masses themselves, but may be used to determine the mass-squared differences $\Delta m^2_{31} = m^2_3 - m^2_1$ and $\Delta m^2_{21} = m^2_2 - m^2_1$. The sign of Δm^2_{31} determines the neutrino mass hierarchy; the "normal hierarchy" (NH) refers to the case in which the mass eigenstate ν_3 is heavier than the other two neutrinos while the case in which ν_3 is lighter than the other two is refereed to as the "inverted hierarchy" (IH). While the mixing angles, the magnitude of the mass-squared differences and the sign of Δm^2_{21} have been determined, the sign of Δm^2_{31} is unknown and the CP-violating phase, δ, is at present essentially unconstrained.

The introduction of neutrino mass requires that the SM be extended. As a minimum, a right-handed neutrino state must be added to accompany the left-handed state. The tiny neutrino mass, so different from those of the other fundamental fermions, hints that the mechanism responsible for neutrino mass is different to the Higgs mechanism by which the quarks and charged leptons acquire mass. To explain, rather than describe, neutrino oscillations requires a theory of the physics of flavour that accommodates the patterns in the observed properties of the fundamental fermions as well as the ways in which the properties of the neutrino differ from those of the quarks and charged leptons. Theories have been constructed in which the patterns observed within a generation are explained by assigning the fermions to a representation of a large symmetry group (Grand Unified Theories, GUTs) and the patterns observed in between or across generations are explained by assuming "family symmetry". Such theories admit an explanation of the tiny neutrino mass and the large neutrino-mixing angles. The "see-saw mechanism", arguably the most attractive scheme to explain the tiny neutrino mass, requires the introduction of extremely heavy, Majorana neutrinos. Such heavy Majorana neutrinos would not feel the weak force—i.e. they would be "sterile neutrinos" incapable of interacting directly with ordinary matter.

Through the see-saw mechanism the properties of the neutrino may be related to physics at extremely large energy scales beyond the reach of present, or realistic future, energy-frontier accelerators. Moreover, in see-saw models, if the heavy Majorana neutrinos are abundant in the early Universe and if the heavy neutrinos decay preferentially to matter fermions, then the lepton-number asymmetry generated in the heavy-neutrino decay would be converted into a baryon asymmetry during the electroweak era. Detailed and precise measurements of the properties of the neutrino are essential for the fascinating particle physics and cosmological phenomena outline above to be elucidated.
Lead author: KL

2 Physics at the Neutrino Factory

2.1 The physics case for advanced neutrino experiments

The unambiguous observation of neutrino oscillations is arguably the most significant development in particle physics of the past two decades [8]. It revealed, beyond reasonable doubt, that neutrinos have mass and that leptons mix. Neutrino masses are not accounted for in the Standard Model of particle physics. It is not hard to modify the Standard Model Lagrangian to accommodate neutrino masses [9]. Indeed, one can write down several different "Standard Neutrino Model" (SνM) Lagrangians that render neutrinos massive that are consistent with the available data. The candidates for the SνM introduce various new degrees of freedom at a variety of energy scales (from below the electron-Volt scale all the way to the Grand Unification scale). Part of the mission of particle-physics experiments in the next few decades will be to elucidate the mechanism by which neutrino mass is generated. The next generation of neutrino experiments will represent a moderate extension of existing techniques. This makes them technologically attractive, since the technical risks are relatively low, but also limits their physics sensitivity. To exploit to the full the discoveries made to date in neutrino physics, advanced neutrino experiments, based on novel technologies, are required. The Neutrino Factory is the ultimate advanced neutrino oscillation facility. In this section, the scientific case for advanced neutrino oscillation experiments in general and of the Neutrino Factory in particular is reviewed.

While the mechanism behind neutrino-mass generation remains unknown, a very successful phenomenological description exists. It considers the existence of three massive neutrinos ν_1, ν_2, and ν_3 with masses m_1, m_2, and m_3, respectively. These mass eigenstates are linear combinations of the "active" neutrino flavours, ν_e, ν_μ, and ν_τ, labelled according to the way they interact with the W-boson and the charged-leptons, e, μ, and τ. One can pick a weak-basis in which neutrinos with a well-defined flavour are related to neutrinos with a well-defined mass via the unitary lepton mixing matrix U: $\nu_\alpha = U_{\alpha i}\nu_i$ ($\alpha = e, \mu, \tau$, $i = 1, 2, 3$). It is customary to define the neutrino masses as follows: $m_1 < m_2$ while m_3 is either the heaviest or the lightest neutrino. To identify m_3, $|m_3^2 - m_1^2|$ and $|m_3^2 - m_2^2|$ are evaluated and the smaller combination is chosen such that it is larger than $m_2^2 - m_1^2$. With the masses labelled in this way, $m_3 > m_2$ if $m_3^2 - m_1^2$ is positive and $m_3 < m_1$ if $m_3^2 - m_1^2$ is negative. Note that $\Delta m_{21}^2 = m_2^2 - m_1^2$ is a positive-definite quantity, while $\Delta m_{31}^2 = m_3^2 - m_1^2$ is allowed to have either sign. It is also customary to refer to the spectrum $m_3 > m_2 > m_1$ as "normal", in which case $\Delta m_{31}^2 > 0$, while the $m_2 > m_1 > m_3$ spectrum is referred to as "inverted," in which case $\Delta m_{31}^2 < 0$. Once the neutrino mass eigenstates are properly defined, it is also customary to parametrise U as prescribed in the Particle Data Book [10]. The neutrino mixing angles (θ_{ij}) are related to the mixing-matrix elements by:

$$\frac{|U_{e2}|^2}{|U_{e1}|^2} \equiv \tan^2\theta_{12}; \quad \frac{|U_{\mu 3}|^2}{|U_{\tau 3}|^2} \equiv \tan^2\theta_{23}; \text{ and } \quad U_{e3} \equiv \sin\theta_{13}e^{-i\delta}; \tag{1}$$

where δ is the CP-odd, "Dirac", phase. Two other CP-odd phases might be required to complete the parametrisation of U if the neutrinos are Majorana fermions. However, these "Majorana" phases can not be observed in neutrino oscillations and will henceforth be ignored. Neutrino-oscillation data are sensitive to the neutrino mass-squared differences, the values of the mixing angles θ_{12}, θ_{13}, θ_{23}, and δ. The experimental results can be succinctly and accurately described by the oscillation of three active neutrinos. For the mass splitting we reach errors of a few percent; however, for all of the mixing angles and the CP phase the errors are in the 10-30% range, see *e.g.* Ref. [11]. Therefore, while three-flavor oscillation is able to describe a wide variety of experiments, it would seem premature to claim that we have entered the era of precision neutrino physics or that we have established the three-flavor paradigm at a high level of accuracy. This is also borne out by the fact that there are significant hints at short baselines for a fourth neutrino [12]. Also, more general, so-called non-standard interactions are not well constrained by neutrino data; for a recent review on the topic see Ref. [13].

Two of the three mixing angles are large, in stark contrast to the quark-mixing matrix, in which all mixing parameters are either small ($\sin\theta_c \sim 0.23$, where θ_c is the Cabibbo angle) or very small ($|V_{ub}| \sim 0.004$). In the neutrino sector, three parameters remain unknown or only poorly constrained: the sign of Δm^2_{31}; δ. At the time of the writing of the interim design report θ_{13} was still unknown, now it has been determined to be large and has been measured to within 10% in $\sin^2\theta_{13}$ [14–16]. This gives existing experiments like T2K [17] and Noνa [18] a chance to determine, in combination, the mass hierarchy. Also new, dedicated experiments like PINGU [19] using atmospheric neutrinos or Daya Bay II [20] using neutrinos from a reactor have a high likelihood to measure the mass hierarchy on a 5-10 year timescale. On somehwat longer timescale LBNE [21] is certain to measure the mass hierarchy. It is also expected that the precision with which $|\Delta m^2_{31}|$ and $\sin^2 2\theta_{23}$ are known will improve significantly. Even under these conditions, it is widely anticipated that by the end of the current decade we shall have no information regarding whether CP-invariance is violated in neutrino interactions ($\delta \neq 0, \pi$).

To complete our knowledge of the parameters that describe neutrino oscillations, the goals of advanced experiments must be:

- To search for CP-invariance violation in neutrino oscillations by seeking to measure the CP-odd phase δ;
- To establish whether the neutrino-mass spectrum is normal or inverted by determining the sign of Δm^2_{31};
- To measure as precisely as possible all the oscillation parameters.

The search for CP-invariance violation in neutrino oscillations provides a unique opportunity to further our understanding of CPx-invariance. Experiments have demonstrated that the CP-odd phase of the quark mixing matrix, $\delta_{\rm CKM}$, controls all CP-invariance violation in the quark sector. The past generation of neutrino-oscillation experiments has revealed that there is at least one more CP-violating parameter in the lepton mixing matrix, δ. In practise, δ can only be observed in neutrino oscillation experiments and an advanced neutrino experiment is required to explore this new window into CP-invariance violation.

Once one realizes that the current error bars are uncomfortably large, the next question is: how well do we want/need to determine the various mixing parameters? The answer can be given at two distinct levels. One is a purely technical one – if I want know X to a precision of x, I need to know Y with a precision of y; an example is, where Y is given by θ_{13} and X could be the mass hierarchy. The answer, at another level, is driven by theory expectations of how large possible phenomenological deviations from the three-flavor framework could be. In order to address the technical part of the question, one first has to define the target precision from a physics point of view. Guidance from other subareas of particle physics reveal that the "target precision" evolves over time. For example, history shows that theoretical estimates of the top quark mass from electroweak precision data and other indirect observable, before its eventual discovery, seem to have been, for the most part (and with very large uncertainties), only several GeV ahead of the experimental reach – at the time, there always was a valid physics argument for why the top quark is "just around the corner." A similar "evolution" of theoretical expectations can be observed in, for example, searches for new phenomena in quark flavor physics. Thus, any argument based on model-building-inspired target precisions is always of a preliminary nature, as our understanding of models evolves over time. With this caveat in mind, one argument for a target precision can be based on a comparison to the quark sector. Based on a theoretical guidance from Grand Unification, one would expect that the answer to the flavor question should find a concurrent answer for leptons and quarks. Therefore, a test of such a models is most sensitive if the precision in the lepton and quark sector is comparable. For instance, the CKM angle γ, which is a very close analog of δ in the neutrino sector, is determined to $(70.4^{+4.3}_{-4.4})^\circ$ [22] and thus, a precision target for δ of roughly 5° would follow.

A different argument for a similar level of precision can be made based on the concept of so-called neutrino sum-rules [23]. Neutrino sum-rules arise, for example, in models where the neutrino mixing matrix has a certain simple form or texture at a high energy scale and the actual low-energy mixing parameters are modified by a non-diagonal charged lepton mass matrix. The simplicity of the neutrino mixing matrix is typically a result of a flavor symmetry, where the overall Lagrangian possesses an overall flavor symmetry G, which can be separated into two sub-groups G_ν and G_l for the neutrinos and charged leptons; it is the mismatch between G_ν and G_l which will yield the observed mixing pattern, see e.g. [24]. Typical candidates for G are given by discrete subgroups of SU(3) which have a three dimensional representation, e.g., A_4. In a model-building sense, these symmetries can be implemented using so-called flavon fields which undergo spontaneous symmetry breaking and it is this symmetry breaking which picks the specific realization of G, for a recent review see [25]. The idea of flavor symmetries is in stark contrast to the idea that neutrino mixing parameters are anarchic, *i.e.* random numbers with no underlying dynamics, for the most recent version of this argument, see Ref. [26]. To find out whether the patterns observed in lepton mixing correspond to an underlying symmetry is one of the prime tasks of neutrino physics. Of course, distinguishing among the many candidate underlying symmetries is also a very high priority.

In practice, flavor symmetries will lead to relations between measurable parameters, whereas anarchy will not. For example, if the neutrino mixing matrix is of tri-bi-maximal form, $|U_{e3}| = 0$ is naively expected to vanish, which is clearly in contradiction to observations. In this case, a non-diagonal charged lepton mass matrix can be used to generate the right value of $|U_{e3}|$, and, for one concrete model, the following sum-rule arises

$$\theta_{12} - \theta_{13}\cos\delta = \arcsin\frac{1}{\sqrt{3}}\,, \tag{2}$$

which can be tested if sufficiently precise measured values for the three parameters $\theta_{12}, \theta_{13}, \delta$ are available. Depending on the underlying symmetry of the neutrino mixing matrix different sum-rules are found. In Fig. 1 several examples are shown and for each case the values of θ_{13} and θ_{12} or θ_{23} are drawn many times from a Gaussian distribution where the mean values and ranges are taken from Eq. **??**. The resulting predictions of the value of the CP phase δ are histogramed and shown as colored lines. The width of the distribution for each sum-rule arises from the finite experimental errors on θ_{12} or θ_{23} and θ_{13}. Two observations arise from this simple

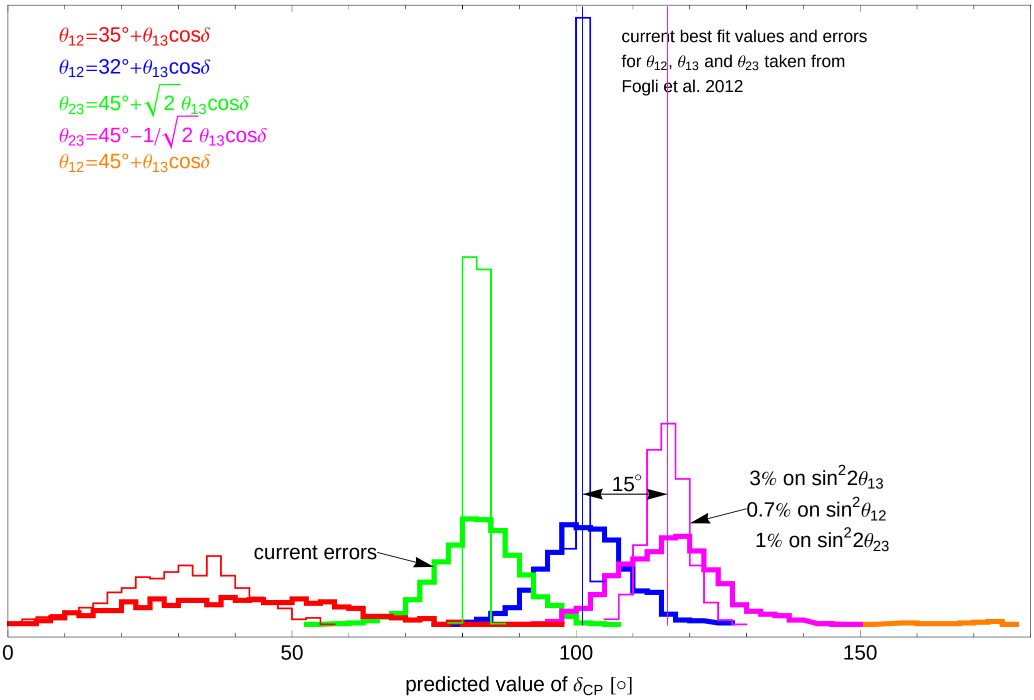

Figure 1: Shown are the distributions of predicted values from δ from various sum-rule as denoted in the legend and explained in the text.

comparison: first, the distance of the means of the distributions is as small as 15°, and second, the width of the distributions is significant compared to their separation and a reduction of input errors is mandated. The thin lines show the results if the errors are reduced to the value given in the plot, which would be achieved by Daya Bay for $\sin^2 2\theta_{13}$, by Daya Bay II for $\sin^2 \theta_{12}$, and by NOvA for $\sin^2 \theta_{23}$. Assuming that the errors on θ_{12}, θ_{23} and θ_{13} are reduced to this level, the limiting factor is the natural spread between models, which is about 15°. A $3\,\sigma$ distinction between models translates into a target precision for δ of 5°. A measurement at this precision would allow to obtain valuable information on whether indeed there is an underlying symmetry behind neutrino mixing. Moreover, it is likely to also provide hints regarding which specific class of symmetries is realized. This would constitute a major breakthrough in our understanding of flavor.

High-precision measurements of neutrino oscillations are required to test whether the origin of neutrino mass is also the origin of the baryon asymmetry of the Universe, through leptogenesis [27, 28]. Several indirect generic predictions of leptogenesis can be verified with neutrino experiments: neutrinos are expected to be Majorana fermions, and it is expected, quite generically, that neutrino oscillations violate CP-invariance, even if no model independent relation between "high-energy" and "low-energy" CP-invariance violation exists. Quantitative tests are all model dependent and will rely on very precise measurements in neutrino oscillations and elsewhere. For example, precise measurements of oscillation parameters could validate a specific flavour model, which allows one to relate "high-energy" and "low-energy" parameters. Furthermore, discoveries at collider experiments and searches for charged-lepton flavour violation may provide other hints that render leptogenesis either "very likely" or "most improbable" [29]. We are very far from testing leptogenesis conclusively, but precise measurements of all neutrino oscillation parameters – far beyond where we are now – are a *conditio sine qua non*.

Precision measurements of the oscillation parameters are also required to confirm or refute with confidence the current three-active-neutrino formalism. Ultimately, one aims not only at constraining the mixing-parameter space, but also at *over-constraining* it. Several important questions need to be addressed:

- Are there really only three light neutrinos and is U a unitary matrix?
- Are there other neutrino interactions? And,
- Is there only one source of CP-invariance violation in the neutrino sector?

While our understanding of the neutrino has increased tremendously over the past decade, we are far from providing a satisfactory answer to any of these questions. In this respect, our understanding of the lepton-flavour sector is far behind our understanding of the quark-flavour sector.

Some manifestations of new physics are best investigated with neutrino oscillation experiments. For example, the search for light sterile neutrinos which may be related to the origin of neutrino masses. Sterile neutrinos can be detected via the observation of new oscillation frequencies and mixing angles. Tests of the unitarity of the lepton-mixing matrix may also point to new "neutrino" degrees of freedom that are too heavy to be seen in oscillation experiments. Neither of these phenomena can be studied outside of neutrino oscillation experiments. Other new-physics ideas to which measurements of neutrino oscillation are uniquely sensitive are related to physics at the electroweak scale, including new four-fermion neutrino interactions (of the current–current type, $\propto (\bar{\nu}_\alpha \Gamma \nu_\beta)(\bar{f}\Gamma' f)$, where f is a charged fermion). Some of these possibilities will be discussed in more detail later in this section. Indeed, non-standard neutrino interactions are often used as proxies for the discussion of the sensitivity of neutrino-oscillation experiments to new physics.

In many candidate new-physics scenarios, a combination of different experimental probes will be required in order to piece together a more fundamental description of how nature works at the smallest distance scales. In addition to studies of neutrino flavour-change, these include collider experiments (for example, the LHC and a next-generation lepton collider), searches for charged-lepton flavour violation in the muon and tau sectors, searches for the permanent electric dipole moments of fundamental particles, including the electron and the muon, searches for lepton-number violation, especially searches for neutrinoless double-beta decay, and direct and indirect searches for dark matter. In many new-physics scenarios, in particular when it comes to identifying the physics responsible for neutrino masses, advanced neutrino oscillation experiments are guaranteed to play a leading role.

Neutrino experiments have proved, over the past few decades, that our ability to predict what will be detected, and to identify what are the important questions, is limited at best. It is safe to state, however, that a Neutrino Factory, combined with a multi-kTon detector at an underground facility, offers a unique and powerful tool for the study of fundamental physics. In order to prepare for the unexpected, it is vital that advanced set-ups be versatile and multifaceted. The Neutrino Factory fits the bill. In addition to providing the neutrino beams required for the definitive, precision neutrino-oscillation programme, the Neutrino Factory also provides an ideal environment in which to study a variety of other phenomena. The well-characterised neutrino beam from the muon storage ring allows a programme of extremely precise neutrino scattering measurements to be carried out at a near detector, including studies of neutrino flavour-change at very short baselines and precision measurements of neutrino scattering on nucleons [30] and electrons [31]. The latter allow for uniquely sensitive tests of the electroweak theory.

Activities not directly related to neutrino physics can also be addressed at a Neutrino Factory complex. The availability of a large number of muons allows one to consider new set-ups for searching for rare muon processes [32], especially $\mu \to e$ conversion in nuclei, and for measurements of the electroweak properties of the muon, including the muon electric and magnetic dipole moments. The availability of a large number of protons—used to make the muons for the storage ring—allows one to consider a suite of hadronic experiments including, for example, those required to study very rare kaon phenomena ($K \to \pi\bar{\nu}\nu$, $K \to \pi\mu^\pm e^\mp$, $K^+ \to \pi^-\ell^+\ell'^+$, etc). At the opposite end of the neutrino beam, the very large detector complex also serves many purposes. Depending on the location and composition, very large detectors can be used to study naturally occurring neutrinos—especially the atmospheric neutrinos and, perhaps, neutrinos from Supernova explosions. Finally, the large instrumented volumes can be used for searching for proton decay. Indeed, the Kamiokande and IMB experiments were originally constructed to look for proton decay, stumbled upon atmospheric neutrino oscillations, and observed neutrinos produced in supernovæ along the way.

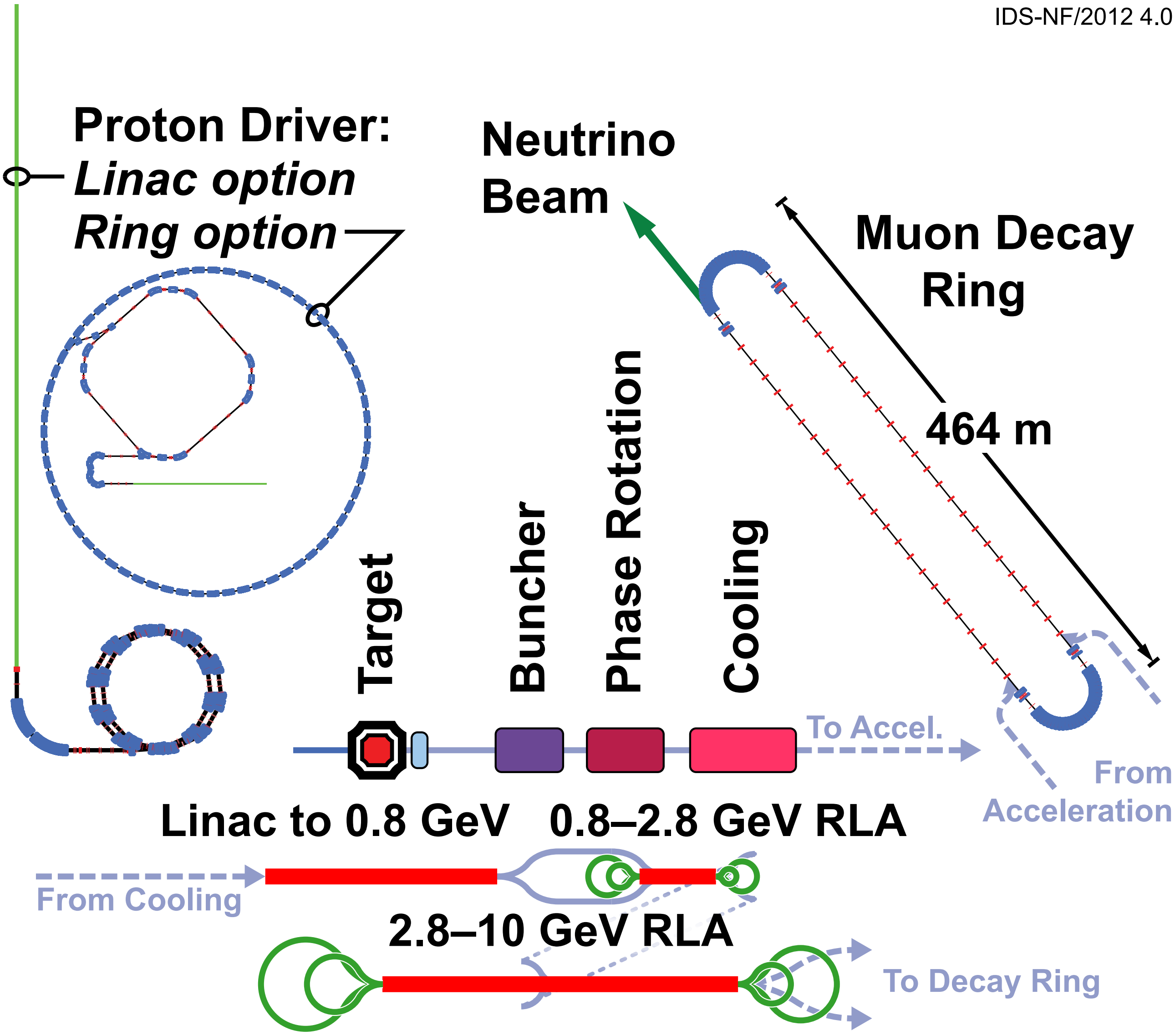

Figure 2: A diagram of the neutrino factory accelerator facility.

3 The Neutrino Factory Accelerator Complex

Lead authors: JSB, JPa

The goal of the accelerator facility is to produce 10^{21} neutrino decays per year from decays of a 10 GeV muon beam. These neutrinos are directed toward a detector at a distance of approximately 2000 km. We first give a short overview of the facility, and then individual subsections will describe the stages in more detail.

The facility begins with a high power proton driver that produces an intense pulsed proton beam. This beam hits a target that produces pions, which then decay into muons. These muons (in the "front end") are manipuled in phase space to produce a train of muon bunches. This bunch train is then accelerated to 10 GeV and injected into a decay ring. The decay ring contains long straights wherein the muons decay into neutrinos, producing the desired neutrino beam.

The proton driver delivers a 4 MW proton beam to the target. This power is required to produce sufficient pions to give us the desired number of neutrino decays. The beam must be sufficiently small to avoid significant reduction in production in the target and capture by the front end. Each proton driver pulse can supply up to 3 bunches; these bunches must be spaced sufficiently to allow them to be accelerated indivudally. More bunches from the proton driver would result in more bunch trains than would fit in the decay ring. We do not specify precisely how we would build a proton driver, since this depends strongly on the existing infrastructure at the laboratory where one would build a neutrino factory. Instead, we present descriptions of how an acceptable proton driver could be built at a couple different laboratories.

The target is a mercury jet. The large atomic number in mercury gives good pion production. Mercury is used since a solid target would likely be damaged by the high proton driver power used here. The target is within a high field solenoid, which allows the capture of both muon signs, and has a large angular acceptance. That solenoid field tapers down as the pions go downstream and begin to decay. A chicane with an absorber at the end is inserted to remove particles other than pions and muons, reducing energy deposition in the downstream systems.

Following the chicane, the remaining pions decay into muons. This is followed by a "Neuffer" buncher and phase rotation, which turns the large energy spread muon beam into a bunch train with a relatively small energy spread. The transverse emittance of this bunch train is then reduced by an ionization cooling channel. The goal of these latter two systems is to create a beam that can be readily accelerated.

The beam is accelerated in three stages in attempted to optimize the acceleration in each energy range. The first stage is a linac accelerating to 0.8 GeV. The subsequent two stages, accelerating to 2.8 and 10 GeV, are 4.5-pass recirculating linear accelerators (RLAs). The use of multiple linac passes in the RLAs increases the acceleration efficiency.

The 10 GeV muon beam is injected into a decay ring. The decay ring has long straights, one of which is pointed toward a detector 2000 km away. The straights are kept long compared to the arcs to ensure that a large fraction of the neutrino decays are toward the far detector. The beam in the straights has a small angular divergence (and therefore a large size) to reduce the uncertainty in the neutrino flux.

3.1 Proton Driver

3.2 Target

Lead authors: KTM

The Target System of the Neutrino Factory is considerably more than the target for the primary proton beam. It includes a high-field solenoid-magnet string for capture of low-energy pions from the target, as well as the infrastructure to house and support the target and capture magnets. Because of the high levels of activation of materials in the Target System, it includes substantial radiation shielding, and remote-handling capability.[6]

Early visions [33] of a target system for a Muon Collider considered (pulsed) toroidal collection (with a Li lens, as at a $\bar{p}$ source), which is limited to one sign of charged particles, and has not been demonstrated for the 50-Hz repetition rate specified for a Neutrino Factory. Pion collection with DC solenoid magnets was proposed in 1995 [34] and has since been the baseline concept. An additional advantage of solenoidal capture in a high-field magnet is that longitudinal-transverse emittance exchange occurs as the field strength decreases adiabatically along the capture channel [35], which provides initial transverse cooling of the secondary pions (at the expense of longitudinal heating). Issues of survival of a solid target in a 4-MW proton beam with $\approx$ 2-ns pulses led to consideration of a free-mercury-jet target [36], now the baseline. Physics feasibility of a mercury-jet target in a strong solenoid field and intense proton pulses was demonstrated in the MERIT experiment at CERN [37].[7]

---

[6] The Final-Focus System of the primary proton beam may or may not be considered as part of the Target System. Also, the string of magnets in the Pion-Decay Channel prior to the Buncher will experience very high radiation loads, so from a technology perspective they are part Target System, although they are described in this document as part of the Front End.

[7] The MERIT experiment did not utilize a continuous-flow of mercury, which has been demonstrated at the Target System of the

Optimisation of particle production at fixed proton-beam power for maximal output of the Neutrino Factory [39] leads to various requirements on the proton driver (Table 1), and on the configuration of the Target System. Useful (low-energy) pion yield from the Hg target peaks at 8 GeV, which is taken to be the baseline value. The desired low-energy pions emerge from the side of the target, which favors a small proton-beam radius, and leads to the (demanding) requirement of geometric transverse emittance of 5 μm for the proton beam. The requirement of short proton bunches (1-3 ns) is based on the need for efficient capture of the secondary beam into rf bunches, so is not strictly a requirement by the Target System.

Table 1: Requirements on the Proton Driver from the Target System. Some parameters correspond to an 8 GeV beam energy.

Parameter	**Value**
Kinetic energy	5–15 GeV
Average beam power	4 MW
	(3.125×10^{15} protons/s)
Repetition rate	50 Hz
Bunches per train	3
Total time for bunches	240 μs
Bunch length (rms)	1–3 ns
Beam radius	1.2 mm (rms)
Rms geometric emittance	< 5 μm
β^* at target	≥ 30 cm

Pion production is maximized when the radius of the jet target is about 3 times that of the proton-beam rms radius, and the proton beam and target have a small tilt with respect to the axis of the capture-solenoid capture. The latter implies that the primary proton beam does not point into the Decay Channel, but off to the side of the Target System, where the mercury-collection pool serves as the beam dump.[8] The proton beam will disrupt the liquid target over most of its effective length ($\approx$ 2 interaction lengths = 30 cm), so the requirement to have a fresh region of the jet at the target at 50 Hz implies the jet velocity must be 20 m/s (which also implies that gravitational curvature of the jet is negligible).

Useful particle production is higher for higher peak magnetic field in the Target System, and 20 T is taken as the baseline value. This is beyond the capability of a Nb-based superconducting magnet, so a hybrid magnet with a 15-T Nb_3Sn outer coil and a 5-T Cu inner coil is specified. Such a hybrid magnet (with 45 T peak field) has been constructed at the NHMFL [40].

The magnetic field in the target system "tapers" down from the peak of 20 T to 1.5 T in the Decay Channel that begins 15 m from the target.

The requirement of dissipation of the 4-MW proton-beam power inside the Target System is a major driver of the system design. Radiation damage to magnet conductors, particularly to organic insulation, limits their useful lifetime to ≈ 10 years of 10^7 operational seconds if the energy deposition by secondary radiation is 0.1 mW/g [41] (sometimes called the ITER limit). Simulations of energy deposition by FLUKA and MARS codes indicate that the inner radius of superconducting coils near the target must be 1.2 m to satisfy the ITER limit, via internal radiation shielding by He-gas-cooled tungsten beads. This large radius implies the magnets of the Target System would have a stored energy of ≈ 3 GJ, comparable to that of the ITER Central Solenoid [42] and the CMS central solenoid [43].

The 5-T Cu coil insert would experience much larger radiation dose, such that organic insulation could not

---

SNS at ORNL [38].

[8] Mitigation is required of splashes in this pool due to the entering mercury jet and the noninteracting part of the proton beam.

be used; rather a MgO-insulated conductor is required, as developed at KEK [44].

Some 15% of the proton-beam energy is transported into the Decay Channel, mostly via scattered beam protons (and protons from nuclear breakup in the target). This requires mitigation via a chicane in the Decay Channel, and implies that the magnets in this channel must also be designed for high radiation dose, as in the Target System.

A vertical section of the Target System is shown in Fig. 3, and the target region, with the 20-T hybrid capture solenoid is shown in more detail in Fig. 4. This magnet module weighs ≈ 200 tons, which sets the scale for the infrastructure required for the Target System.

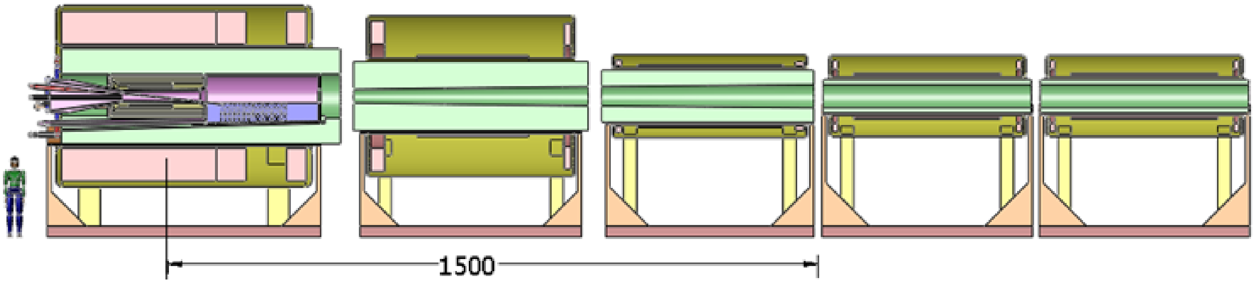

Figure 3: Vertical section of the three magnet modules of Target System (which nominally ends at $z = 1500$ cm) and the first two modules of the Decay Channel.

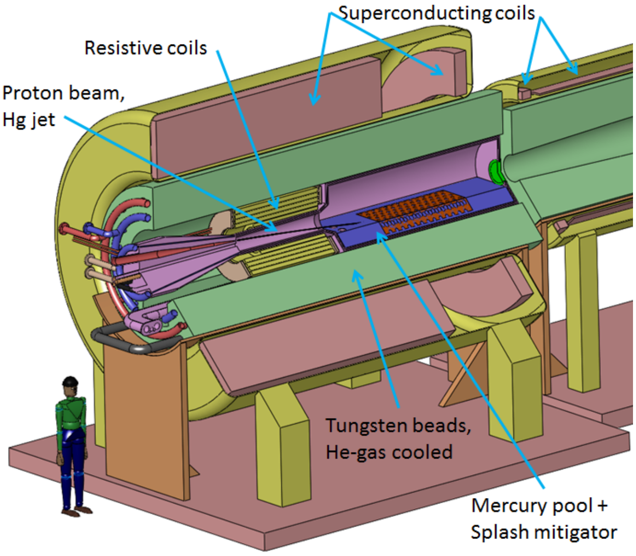

Figure 4: View of the 200-ton 20-T capture solenoid, with internal shielding by tungsten beads. The free-mercury jet target and the proton beam are tilted with respect to the magnetic axis, and impinge on the mercury-collection pool that also serves as the proton beam dump.

3.3 Front End

The Neutrino Factory muon front-end captures pions produced on the target by means of a pion decay channel and particle selection system followed by a longitudinal drift to an adiabatic buncher, energy-phase rotation system and ionisation cooling channel. Subsequently the beam enters the muon accelerator chain. A schematic of the front end is shown in fig. 5.

The present design is based on the lattice presented in the Neutrino Factory Study 2A report [45] and subsequently developed in the International Scoping Study for a Neutrino Factory (ISS) [46] and EuroNu design report [**?**].

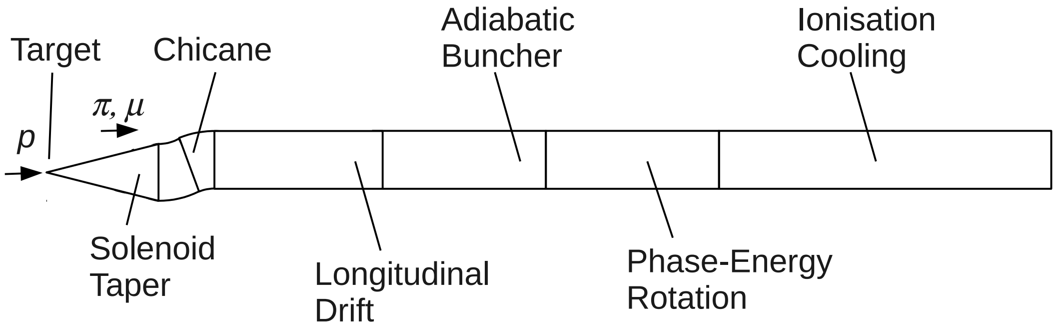

Figure 5: Schematic diagram of the muon front end.

3.3.1 Baseline Overview

Pions are captured in a solenoidal field that tapers adiabatically from 20 T to 1.5 T while the beam pipe radius increases from 0.075 m to 0.30 m over a distance of about 15.0 m. A large transverse phase space of both positively and negatively charged particles with a large energy spread is captured in the solenoidal field.

A chicane follows at 19.0 m, consisting of a 5.0 m outward bend followed by a 5.0 m reverse bend. Each bend has bending angle of 12.5^o and radius of curvature of 22.9 m, with the bending field made using a 1.5 T toroidal solenoid. The chicane is designed to remove particles with momentum above 500 MeV/c. A 0.1 m long Beryllium plug is placed after the chicane to range out low energy protons that remain in the beam.

The beam continues in the 1.5 T field for another 40.9 m with no RF, giving rise to a time-energy correlation. The beam then passes through 44 RF cavities, each of which has frequency selected to be synchronous with particles in the beam despite the growing separation due to time of flight variation with energy. Cavities are 0.5 m long and each is separated by 0.25 m vacuum. The voltage of each cavity is higher than the previous to enable a pseudo-adiabatic formation of a bunch train. This leads to cavities with frequencies of 358.92 MHz at the start to 235.40 MHz at the end of the buncher and gradients up to 11.904 MV/m.

Once the voltage has reached its nominal peak value and bunches have formed, the cavities are slightly dephased so that fast muons at the head of the bunch experience a decelerating phase and slow muons at the tail of the bunch experience an accelerating phase. The phase is chosen so that the head bunch and tail bunch have the same energy when the bunch frequency is 201.25 MHz, with a gradient of 13.0 MV/m used throughout the energy-phase rotation system.

Subsequently the beam enters an ionisation cooling channel. The muons are passed through an absorber reducing both transverse and longitudinal momentum. They are then reaccelerated in an RF cavity, replacing momentum in only the longitudinal direction resulting in a reduction of transverse emittance. Multiple Coulomb scattering and energy straggling tend to create noise counteracting the emittance reduction. A low-Z material is chosen for the absorber to minimise these effects.

The beam is matched from the constant 1.5 T field to a field that alternates from +2.8 T to -2.8 T with a period of 0.86 m. Cooling modules are grouped into a series of 5 RF cavities separated by a vacuum region. Superconducting coils are placed between each RF cavity to provide the alternating field. Each RF cavity has a length of 0.5 m, with 9 mm thick, Beryllium-coated Lithium Hydride windows that perform the ionisation cooling and additionally provide an electromagnetic seal to the cavity improving the real estate gradient. The RF cavities operate at 16 MV/m and 35^o phase, with a frequency of 201.25 MHz. Each 5-cavity assembly is followed by a magnetic cell with no RF cavity, allowing space for bellows and other equipment.

3.3.2 Capture Performance

The capture performance of the muon front end is shown in fig. 6. Overall, 0.066 good μ^+ are captured per 8 GeV proton on target. Muons are considered to be good if they fall within a momentum range of 100 to 300 MeV/c, a normalized transverse 4D amplitude of 30 mm and a longitudinal 2D amplitude of 150 mm. This is considered to be the nominal acceptance of the accelerator system.

In 2D, normalized amplitude is $a^2mc/(\beta p)$, where a is the transverse size of the matched phase space ellipse on which the particle lies, m is the particle mass, β is the Courant-Snyder beta function, and c is the speed of light. The normalized transverse 4D amplitude is the sum of the horizontal and vertical transverse amplitudes, modulo correlations. The normalized longitudinal amplitude is the equivalent quantity for the longitudinal plane, which is approximately $(\Delta E)(\Delta t)/(mc)$, where ΔE is the energy difference from the average momentum, and δt is the time difference from the average time (where all bunches are aliased onto a single bunch). The calculation used for this study is more formally defined in [**?**].

A rapid loss of particles from the good region after 20 m can be attributed to the effect of the proton absorber. The number of particles within the good region increases rapidly in the phase rotator, with a more leisurely rise in the ionisation cooling section.

3.3.3 Activation of Components

Energy deposition has been identified as a serious issue in the muon front end, and a particle selection system has been designed to constrain the majority of hadronic losses in an active handling area near to the target region.

The efficacy of the particle selection system is demonstrated in fig. 7. The particle selection system reduces uncontrolled protonic losses by 2 orders of magnitude. Nonetheless 1.2 kW of proton beam power is lost outside of the active handling region, with roughly 0.2 kW lost at the interface between the phase rotator and cooler.

3.4 Acceleration

3.4.1 Introduction

Here we present a scheme to accelerate muons from the end of the cooling channel (244 MeV) to about 10 GeV - the energy required by the Neutrino Factory under study. To ensure an adequate survival rate for the short-lived muons, acceleration must occur at high average gradient. The accelerator must also accommodate the phase-space volume occupied by the beam after the cooling channel, which is still large [Ref. Cooling

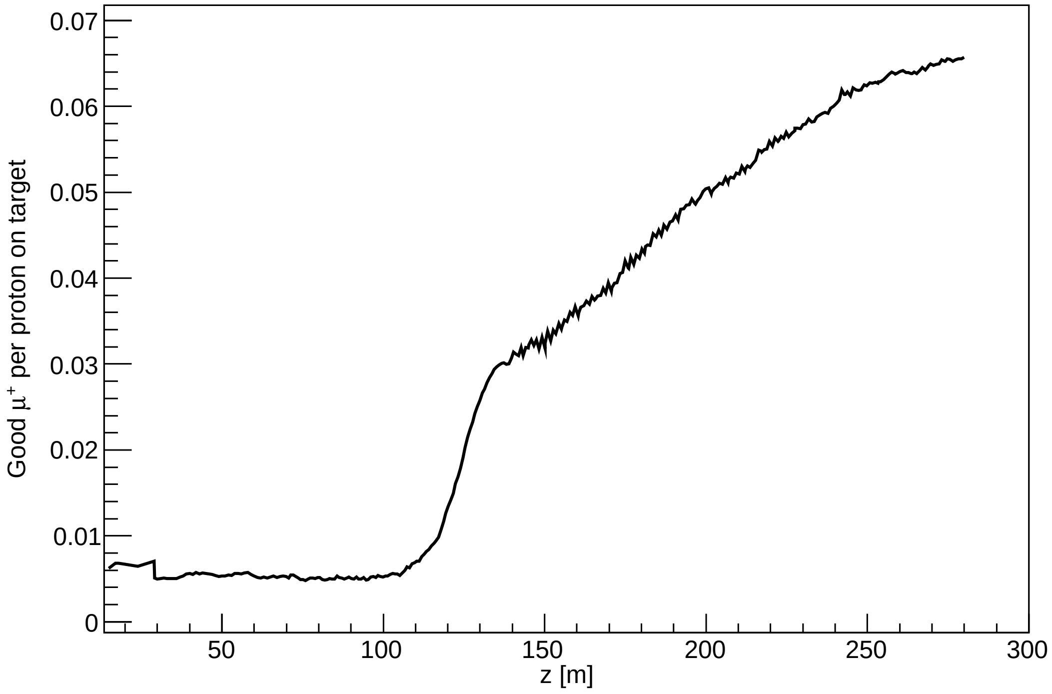

Figure 6: Number of muons captured by the front end, as simulated in ICOOL v3.20. TODO: negatives; error bars; G4BL capture, (G4BL version)

Channel Sec]. The need for large transverse and longitudinal acceptances drives the design of the acceleration system to low RF frequency, e.g. 201 MHz. High-gradient normal conducting RF cavities at these frequencies require very high peak power RF sources. Hence Superconducting RF (SRF) cavities are preferred. In the following we choose a SRF gradient of 15-17 MV/m, which will allow survival of about 85% of the muons as they are accelerated to 10 GeV.

3.4.2 Accelerator Complex

The proposed muon accelerator complex consists of a single-pass, 201 MHz SRF linac, that captures the large muon phase space coming from the cooling channel. The Pre-linac accelerates the muons to sufficiently relativistic energies (775 MeV kinetic energy) to facilitate efficient multi-pass acceleration in the RLA, while adiabatically decreasing the phase-space volume. The large acceptance of the linac requires large aperture (23 cm radius) and tight focusing. This combined with moderate beam energies favors solenoidal rather then quadrupole focusing for the entire linac. The Pre-linac is followed by the first Recirculating Linear Accelerator (RLA I) that further compresses and shapes the longitudinal and transverse phase-space, while increasing the energy to 2.8 GeV in in 4.5 passes. The beam is injected at the middle of 850 MeV SRF linac to minimize the effect of phase slippage for initially 0.8 GeV muon beam accelerated in a linac phased for the speed-of-light particle. In a “Dogbone” RLA the beams at the ends of the linac need to be directed into the appropriate energy-dependent “droplet” arcs (4) for recirculation. Finally, the RLA I is followed by the second, 4.5 pass RLA, based on 1.6 GeV SRF linac, that accelerates muons to 10 GeV. All linacs are based on 201 MHz SRF cavities; with the Pre-linac utilizing large aperture (23 cm radius), lower gradient (15 MV/m) cavity design,

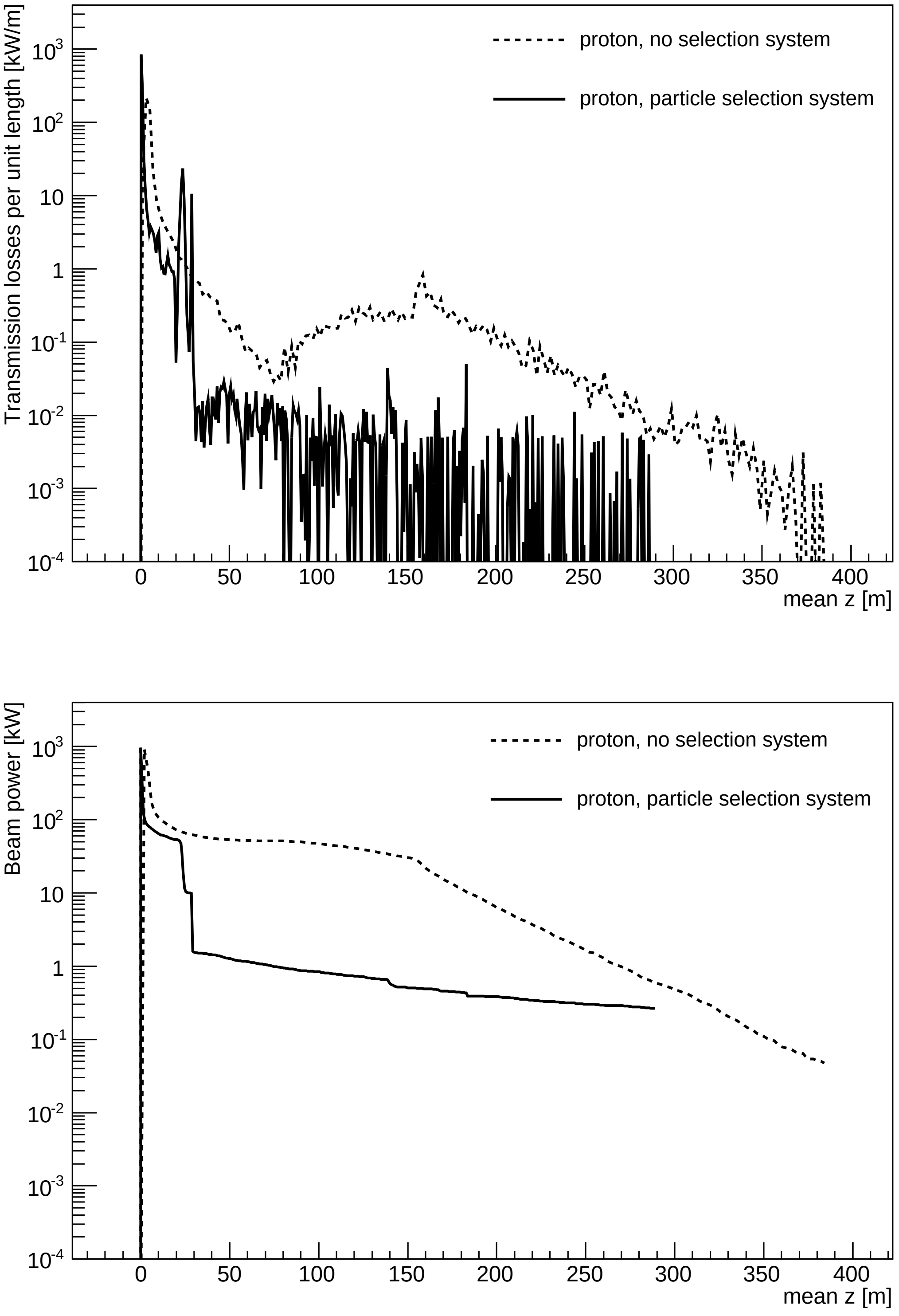

Figure 7: The (top) transmission losses of protons and (bottom) residual proton beam power in the muon front end are shown, as simulated in G4Beamline v2.06. (Dashed) without a particle selection system (Full) with the chicane and proton absorber as a particle selection system.

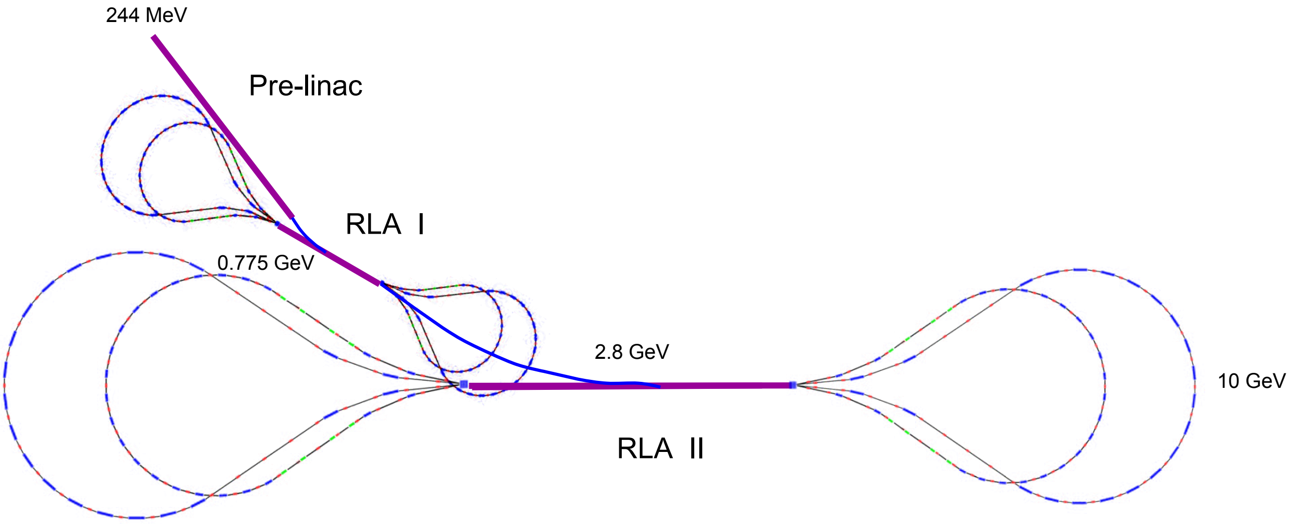

Figure 8: Layout of the accelerator complex: a single-pass Pre-linac to 0.775 GeV followed by a pair of 4.5-pass "Dogbone" RLAs: to 2.8 GeV and 10 GeV.

while RLA I and RLA II are configured with smaller aperture (15 cm radius), higher gradient (17 MV/m) cavities

For practical civil engineering reasons the in-plane horizontal layout of all three components is favored rather than a vertically stacked, somehow more compact configuration. All three accelerators are connected by compact transfer lines, configured as vertically separated double arcs, capable of transferring both charge species between consecutive acceleration stages.

The overall layout of the accelerator complex is shown in Fig. 8.

3.5 Decay Ring

In the Neutrino Factory [46] neutrinos are generated from muon decays according to:

$$\mu^- \to e^- \bar{\nu}_e \nu_\mu \,; \text{ and } \mu^+ \to e^+ \nu_e \bar{\nu}_\mu \,. \tag{3}$$

Neutrinos are aimed at near and far detectors by collecting muons a storage ring with long straight sections pointing at a distant experimental facility. The storage ring dips into the ground with an angle of 9° for a 2000 km baseline.

Since the decay ring needs to serve a single baseline, a racetrack geometry, which can direct neutrinos resulting from the decays of both muon charges to the same far detector, is the logical option (triangular and bow-tie rings were considered in the IDR to serve two baselines). The racetrack ring is designed to store counter-rotating muon bunches with each long straight serving as production sections for either μ^+ or μ^-. The neutrino production efficiency η_p is defined as the length of the production straight divided by the ring circumference. In this design η_p is 35.56% which is a reasonable tradeoff between physics, geology considerations and cost.

There will be at most three μ^+ and three μ^- bunch trains in the ring. The bunch trains, 250 ns long at injection, will debunch due to their finite momentum spread and the non-zero phase-slip in the ring. Until the muon bunches have decayed in sufficient numbers, a 100 ns gap between the neutrino bursts arising from the μ^+ and the μ^- bunches should be maintained. In addition, the circumference must be large enough to allow sufficient rise/fall time for the injection kickers. Finally, there should be a rational relation between the orbit periods of the proton driver and the decay ring to ensure equal spacing of the injected bunches.

The optical properties of the ring are challenging. In order to keep the neutrino flux uncertainty sufficiently small, the rms divergence of the muon beam in the production straight section must not exceed 10% of the natural angular divergence of $1/\gamma$ that arises from the kinematics of muon decay. This requirement translates into high values for the β-functions in the production straights (~ 70 m) which need to be matched into the low values of ~ 14 m in the arcs. At the ends of each straight, small bending magnets are included to ensure that neutrinos created in the matching section (where the muon beam still has a large divergence angle) cannot be seen by the detector.

In order to allow a realistic injection scenario, a dedicated injection insertion is included. Injection into the production section is challenging owing to the low phase advance per cell and large transverse β, leading to high kicker peak fields and aperture requirements. Injecting into the arc is precluded since the elements there are tightly packed. A dedicated dispersion-free injection section is therefore located between the matching to the production straight and the arc.

From the center of the upper (closest to the surface) to the center of the lower arc, the ring structure is:

- Upper arc using FODO cells
- Dispersion suppression section, like the arc cells but with different dipoles
- Matching section
- Injection section with a triplet structure
- Matching section with a small amount of bend
- Production straight using FODO cells
- Matching section with a small amount of bend
- Lower arc

The lattice is reflection-symmetric about the centers of the arcs. Figure 9 gives a diagram of the ring. The principal ring parameters are listed in Table 2. Assuming the total momentum spread is given by $\delta = 0.05$, the beam can circulate for ten mean decay times before the neutrino signal gap drops below 100 ns.

Figure 9: Decay ring geometry. The injection point is indicated.

Table 2: Ring Parameters

Production straight	562.0×2	m
Upper arc (incl. disp supp)	121.155	m
Lower arc	112.729	m
Insertion	46.4×2	m
Matching sections (total)	104.987	m
Circumference	1555.672	m
Width of ring	74.565	m
Length of ring	737.228	m
Angle of inclination	10	deg
Maximum depth of ring	128.02	m
Production efficiency η_p	$36.1\% \times 2$	
Total tune (H,V)	14.77, 13.73	
Chromaticity (H,V)	-17.11, -20.23	
Phase slip η	2.8×10^{-3}	
Turns per mean lifetime	40.07	

4 Detector systems for the Neutrino Factory

Lead authors: PS, ABr, JM, RT

5 Conclusions

Lead author: KL

Acknowledgements

Lead author: KL

References

[1] **IDS-NF** Collaboration, "The International Design Study for the Neutrino Factory.". https://www.ids-nf.org/wiki/FrontPage.

[2] "Ninth International Workshop on Neutrino Factories, super-beams, and beta-beams.". http://fphy.hep.okayama-u.ac.jp/nufact07/.

[3] **IDS-NF** Collaboration, The Steering Group on behalf of the collaboration, "Principal objectives.". https://www.ids-nf.org/wiki/FrontPage/Documentation?action=AttachFile&do=get&target=IDS-NF-001-v1.0.pdf.

[4] B. Pontecorvo, "Mesonium and antimesonium," *Sov. Phys. JETP* **6** (1957) 429.

[5] B. Pontecorvo, "Inverse beta processes and nonconservation of lepton charge," *Sov. Phys. JETP* **7** (1958) 172–173.

[6] Z. Maki, M. Nakagawa, and S. Sakata, "Remarks on the unified model of elementary particles," *Prog. Theor. Phys.* **28** (1962) 870–880.

[7] S. M. Bilenky, S. Pascoli, and S. T. Petcov, "Majorana neutrinos, neutrino mass spectrum, CP-violation and neutrinoless double beta-decay. I: The three-neutrino mixing case," *Phys. Rev. D* **64** (2001) 053010, `arXiv:0102265 [hep-ph]`.

[8] M. C. Gonzalez-Garcia and M. Maltoni, "Phenomenology with Massive Neutrinos," *Phys. Rept.* **460** (2008) 1–129, `arXiv:0704.1800 [hep-ph]`.

[9] R. Mohapatra, S. Antusch, K. Babu, G. Barenboim, M. Chen, *et al.*, "Theory of neutrinos: A White paper," *Rept. Prog. Phys.* **70** (2007) 1757–1867, `arXiv:hep-ph/0510213 [hep-ph]`.

[10] **Particle Data Group** Collaboration, K. Nakamura *et al.*, "Review of particle physics," *J. Phys. G* **G37** (2010) 075021.

[11] G. Fogli, E. Lisi, A. Marrone, D. Montanino, A. Palazzo, *et al.*, "Global analysis of neutrino masses, mixings and phases: entering the era of leptonic CP violation searches," *Phys.Rev.* **D86** (2012) 013012, `arXiv:1205.5254 [hep-ph]`.

[12] K. Abazajian *et al.*, "Light Sterile Neutrinos: A White Paper," `arXiv:1204.5379 [hep-ph]`.

[13] T. Ohlsson, "Status of non-standard neutrino interactions," *Rep. Prog. Phys. 76,* **044201** (2013) 044201, `arXiv:1209.2710 [hep-ph]`.

[14] **Double Chooz Collaboration** Collaboration, Y. Abe *et al.*, "Reactor electron antineutrino disappearance in the Double Chooz experiment," *Phys.Rev.* **D86** (2012) 052008, `arXiv:1207.6632 [hep-ex]`.

[15] **RENO collaboration** Collaboration, J. Ahn *et al.*, "Observation of Reactor Electron Antineutrino Disappearance in the RENO Experiment," *Phys.Rev.Lett.* **108** (2012) 191802, `arXiv:1204.0626 [hep-ex]`.

[16] F. An, J. Bai, A. Balantekin, H. Band, D. Beavis, *et al.*, "Observation of electron-antineutrino disappearance at Daya Bay," `arXiv:1203.1669 [hep-ex]`. 5 figures.

[17] Y. Itow *et al.*, "The JHF-Kamioka neutrino project," *Nucl. Phys. Proc. Suppl.* **111** (2001) 146–151, `arXiv:0106019 [hep-ex]`.

[18] **NOvA Collaboration** Collaboration, D. Ayres *et al.*, “NOvA: Proposal to build a 30 kiloton off-axis detector to study nu(mu) –¿ nu(e) oscillations in the NuMI beamline,” `arXiv:hep-ex/0503053 [hep-ex]`.

[19] **PINGU collaboration** Collaboration, T. IceCube, “PINGU Sensitivity to the Neutrino Mass Hierarchy,” `arXiv:1306.5846 [astro-ph.IM]`.

[20] Y. Wang, “Daya bay ii: current status and future plan.” talk at Daya Bay II meeting, IHEP, Jan, 2013.

[21] **LBNE Collaboration** Collaboration, T. Akiri *et al.*, “The 2010 Interim Report of the Long-Baseline Neutrino Experiment Collaboration Physics Working Groups,” `arXiv:1110.6249 [hep-ex]`.

[22] A. Lenz, U. Nierste, J. Charles, S. Descotes-Genon, H. Lacker, *et al.*, “Constraints on new physics in $B - \bar{B}$ mixing in the light of recent LHCb data,” *Phys.Rev.* **D86** (2012) 033008, `arXiv:1203.0238 [hep-ph]`.

[23] S. King, “Predicting neutrino parameters from SO(3) family symmetry and quark-lepton unification,” *JHEP* **0508** (2005) 105, `arXiv:hep-ph/0506297 [hep-ph]`.

[24] G. Altarelli and F. Feruglio, “Discrete Flavor Symmetries and Models of Neutrino Mixing,” *Rev.Mod.Phys.* **82** (2010) 2701–2729, `arXiv:1002.0211 [hep-ph]`.

[25] S. F. King and C. Luhn, “Neutrino Mass and Mixing with Discrete Symmetry,” `arXiv:1301.1340 [hep-ph]`.

[26] A. de Gouvea and H. Murayama, “Neutrino Mixing Anarchy: Alive and Kicking,” `arXiv:1204.1249 [hep-ph]`.

[27] M. Fukugita and T. Yanagida, “Baryogenesis Without Grand Unification,” *Phys. Lett.* **B174** (1986) 45.

[28] S. Davidson, E. Nardi, and Y. Nir, “Leptogenesis,” *Phys. Rept.* **466** (2008) 105–177, `arXiv:0802.2962 [hep-ph]`.

[29] M. Buckley and H. Murayama, “How can we test seesaw experimentally?,” *Phys. Rev. Lett.* **97** (2006) 231801, `arXiv:hep-ph/0606088 [hep-ph]`.

[30] M. L. Mangano *et al.*, “Physics at the front end of a neutrino factory: A Quantitative appraisal,” `arXiv:0105155 [hep-ph]`. Report of the nuDIS Working Group for the ECFA-CERN Neutrino-Factory study.

[31] A. de Gouvêa and J. Jenkins, “What can we learn from neutrino electron scattering?,” *Phys. Rev. D* **74** (2006) 033004, `arXiv:0603036 [hep-ph]`.

[32] J. Aysto *et al.*, “Physics with low-energy muons at a neutrino factory complex,” `arXiv:0109217 [hep-ph]`. Report of the Stopped Muons Working Group for the ECFA - CERN study on Neutrino Factory and Muon Storage Rings at CERN.

[33] D. Neuffer, “Design of muon storage rings for neutrino oscillation experiments,” *IEEE Trans. Nucl. Sci.* **28** (1981) 2034.

[34] R. C. Fernow *et al.*, “Targets and magnetic elements for pion collection in muon collider drivers,” *AIP Conf. Proc.* **352** (1995) 134.

[35] R. Chehab, “A second order calculation of the adiabatic invariant of a charged particle spiraling in a longitudinal magnetic field,” *J. Math. Phys.* **19** (1978) 937.

[36] R. B. Palmer *et al.*, “Muon colliders,” *AIP Conf. Proc.* **372** (1996) 3.

[37] K. T. McDonald *et al.*, “The MERIT high-power target experiment at the CERN PS,” in *Proceedings of IPAC’10, Kyoto, Japan*, p. 3527. IPAC’10/ACFA, 2010.

[38] T. McManamy *et al.*, “Overview of the SNS target system testing and initial beam operation experience,” *J. Nucl. Mat.* **377** (2008) 1.

[39] X. Ding *et al.*, “Optimized parameters with a mercury jet target,” in *Proceedings of PAC09, Vancouver, BC, Canada*, p. 2748. 2009.

[40] M. D. Bird *et al.*, “The NHMFL hybrid magnet projects,” *IEEE Trans. Appl. Supercon.* **19** (2009) 1612.

[41] J. H. Schultz, “Radiation resistance of fusion magnet materials,” in *20th IEEE/NPSS Symposium on Fusion Engineering, 2003*, p. 423. IEEE, 2003.

[42] J. H. Schultz *et al.*, “The ITER central solenoid,” in *Twenty-First IEEE/NPSS Symposium on Fusion Engineering, 2005*. IEEE, 2005.

[43] A. Hervé *et al.*, “Experience gained from the construction, test and operation of the large 4-T CMS coil,” *IEEE Trans. Appl. Supercon.* **18** (2004) 346.

[44] K. H. Tanaka *et al.*, “Development of radiation resistant magnets for JHF/J-PARC,” *IEEE Trans. Appl. Supercon.* **14** (2004) 402.

[45] **Neutrino Factory/Muon Collider** Collaboration, C. Albright *et al.*, “The neutrino factory and beta beam experiments and development,” (2004) , `physics/0411123`.

[46] **ISS Accelerator Working Group** Collaboration, M. Apollonio *et al.*, “Accelerator Design Concept for Future Neutrino Factories,” *JINST* **4** (2009) P07001.

[47] **ISS Physics Working Group** Collaboration, A. Bandyopadhyay *et al.*, “Physics at a future Neutrino Factory and super-beam facility,” *Rept. Prog. Phys.* **72** (2009) 106201, `arXiv:0710.4947 [hep-ph]`.

[48] Muon Accelerator Program, “Muon accelerator program snowmass whitepaper,” 2013. in preparation.

[49] E. Christensen, P. Coloma, and P. Huber, “Physics Performance of a Low-Luminosity Low Energy Neutrino Factory,” `arXiv:1301.7727 [hep-ph]`.

[50] `HTTP://WWW-AP.FNAL.GOV/MARS/`.

[51] “Mad-x.” `HTTP://MAD.HOME.CERN.CH/MAD/`.

A Incremental Development of a 10 GeV Neutrino Factory

Chris Rogers, Patrick Huber

The Neutrino Factory facility will provide an intense beam of high energy neutrinos for precision measurement of CP violation. Here a series of stages are examined that may permit incremental development of a facility with physics at each stage and with a relatively small increase in the overall facility cost. The advantage of constructing such a facility incrementally is that it may be easier to fit within presumed funding profiles and the technical risk can be spread more evenly over the project lifetime.

A.1 Neutrino Factory baseline

The Neutrino Factory facility baseline design makes a beam of muons by firing a high power and short pulse proton beam onto a target. The resultant secondary particles contain many charged pions along with other secondaries. These pions are captured into a solenoidal field, during which most decay to muons. Subsequently the muons are taken through a solenoidal chicane and proton absorber to remove protons and particles outside the momentum acceptance of the capture system.An adiabatic buncher and phase rotator is used to capture muons longitudinally. Transverse ionisation cooling is used to reduce the transverse emittance of the muon beam, leading to the capture of a significant number of useful muons.

In the baseline design, these muons are subsequently accelerated in a linac from 0.2 GeV to 0.8 GeV; and in two RLAs, first from 0.8 GeV to 2.8 GeV and secondly from 2.8 GeV to 10 GeV.

The muons are finally injected into a storage ring at 10 GeV where they decay into neutrinos and electrons. The neutrino decay products are directed towards a remote detector where the flux of different neutrino species can be measured.

In this paper the Neutrino Factory baseline is considered the final design goal of the facility, and staging schemes are considered that would deliver this facility as the final stage.

A.2 Staging Schemes

In this paper, the number of neutrino interactions is considered as the means to providing an incremental approach to a Neutrino Factory facility.

The number of neutrino interactions can be modified either by modifying the number of muons reaching the storage ring, typically by modifying the design of the capture channel; or by reducing the detector size.

The scheme chosen is driven by a balance between physics need, cost and perceived technical risk. Delaying the construction of certain elements can spread cost and risk more evenly over the project lifetime. It is perceived that, for example, gaining experience with muon beam handling and radiation issues with a low rate beam may enable a better design and lower risk associated with higher rate beams.

A.3 Rate Staging

More than half of the projected Neutrino Factory cost is associated with the proton driver and capture section, which are the sections that mostly impact the rate of muons in the storage ring. Additionally, these are expected to be the most technically challenging parts of the Neutrino Factory design, while the accelerator and decay ring designs are expected to be relatively low risk.

It is proposed that an initial stage would be using a lower power proton driver, possibly at an existing facility, a target horn rather than high field capture solenoid and no cooling section. An upgrade scenario would then be to build a high field solenoid in the capture region, extend the beamline adding a cooling section and as a further stage to increase the proton driver beam power to 4 MW.

Implementing a staged scenario in this way is challenging due to the practicalities of manipulating highly activated targets and beam transport lines. Conventional transport elements like bending magnets would result in a dramatically reduced beam transport due to the exceptionally large beam emittance, both transverse and longitudinal, which cannot be transported efficiently by multipole-type lattices [**?**] [**?**].

In this study a solenoidal chicane is proposed to introduce a transverse displacement. A schematic diagram of the proposed scheme is shown in Fig. 10.

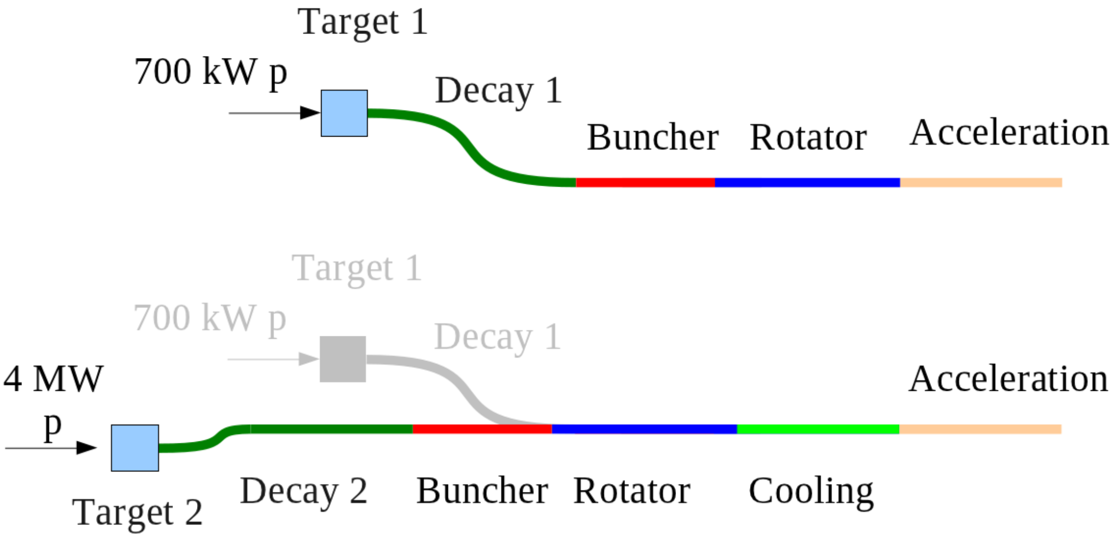

Figure 10: Schematic diagram of (top) stage 1 and (bottom) stage 2 and 3 of the proposed scheme. Stage 3 is to increase the proton beam power on target to 4 MW.

A.3.1 Muon Chicane to Create Transverse Displacement

The muon chicane mentioned above, is designed to remove undesirable secondaries from the beam. A solenoidal chicane is used which has excellent properties for transport of high emittance beams.

Increasing the radius of curvature of the chicane increases the lateral displacement of the beam pipe without significantly affecting the beam transport properties.

A.3.2 Magnetic Field in a Constant Radius Constant Field Bent Solenoid

The magnetic field in a bent solenoid is assumed to have only a radial dependence, such that it can be written as

$$\mathbf{B}_{bs} = f(\rho)\mathbf{s} \tag{4}$$

From Maxwell's equations, in the absence of current sources

$$\begin{aligned}\nabla \times \mathbf{B} &= (\frac{1}{\rho}\partial_s B_y - \partial_y B_s)\rho + \\ &\quad (\partial_y B_\rho - \partial_\rho B_y)\mathbf{s} + \\ &\quad \frac{1}{\rho}(\partial_\rho \rho B_s - \partial_s B_\rho)\mathbf{y} = 0.\end{aligned}$$

Substituting for $\mathbf{B}_{bs}$ gives

$$\partial_\rho \rho f(\rho) = 0 \tag{5}$$

which has the solution

$$f(\rho) = \frac{b_0}{\rho} = \frac{b_s \rho_0}{\rho}. \tag{6}$$

Here b_s is the magnetic field strength on the reference orbit at radius ρ_0.

A.3.3 Helical Motion

In the presence of a field of this nature, some particles can be shown to travel in a helix. Starting from the Lorentz equations,

$$\mathbf{F} = \frac{d\mathbf{p}}{dt} = q\mathbf{v} \times \mathbf{B} \tag{7}$$

it is possible to derive the criterion for helical motion. Assume no radial velocity, so that

$$\mathbf{v} = c\frac{p_y \mathbf{y} + p_s \mathbf{s}}{E} \tag{8}$$

with speed of light c. Then if the particle is travelling at radius ρ

$$\mathbf{F} = qc\frac{p_y b_0}{E\rho} \tag{9}$$

For circular or helical motion, with constant energy,

$$\mathbf{F} = m\gamma\rho\omega^2 = \frac{m\gamma\beta_s^2 c^2}{\rho} = \frac{c^2 p_s^2}{E r_0}. \tag{10}$$

By equating the two expressions for $\mathbf{F}$

$$\frac{c^2 p_s^2}{E\rho} = qc\frac{p_y b_0}{E\rho}. \tag{11}$$

Then if

$$p_y = \frac{q p_s^2}{b_0} \tag{12}$$

particle motion will be on a helix. It should be noted that the slope of the helix is independent of the radius.

A.3.4 Vertical Displacement

In a chicane-type geometry vertical displacement into a collimator used to reject high momentum particles. The vertical displacement is given by

$$\delta_y = \frac{dy}{ds}\delta_s \tag{13}$$

where δ_s is the total path length through the circular orbit,

$$\delta_s = \rho\delta_\theta \tag{14}$$

and δ_θ is the total bend angle of the chicane. The vertical divergence is given by

$$\frac{dy}{ds} = \frac{p_y}{p_s} = \frac{qp_s}{b_0} \tag{15}$$

so

$$\delta_y = \frac{qp_s}{b_0}\rho\delta_\theta = \frac{qp_s}{b_s}\delta_\theta \tag{16}$$

and the vertical displacement is independent of the radius of the helix. This is a useful feature as the chicane radius of curvature can be increased to provide a larger transverse displacement of the beam pipe. This may provide space for the beam pipe and tunnel to pass from the second target station, past the decommissioned first target station and into the existing tunnel for acceleration.

A.3.5 Tracking through a Dual Chicane System

The effect of introducing a second chicane was studied in a full Monte Carlo simulation. In this study, the initial 10 m long chicane, used for removing undesirable pollutants from the beam, was left in situ and a second, 40 m long chicane was placed immediately after the proton absorber, replacing almost all of the drift section with a chicane. The total bending angle in each half of both chicanes was left unchanged at $12.5°$, resulting in a radius of curvature of 22.9 m and 91.7 m respectively and a horizontal transverse displacement of 1.08 m and 4.34 m respectively.

The tracking results for the two front ends are shown in Fig. 11. There is a slight degradation in capture performance, with peak muon yield reduced from 0.0672 muons per proton to 0.06495 muons per proton. (TODO: update that number on final design; errors?)

By introducing a second chicane, it is possible to introduce a lateral displacement of the target region that would enable a target station upgrade as part of the staging scheme.

A.3.6 Removing the cooling channel

Removal of the cooling channel would necessitate moving, reinstalling and recommissioning the buncher and phase rotator in an upstream position. While this may be time consuming, the dominant cost of the front end is in the capital cost of RF power supplies and so it is thought that it will only increment the total cost by a small fraction. It would, however, necessitate rebuilding the target station and initial capture region as following operation of the facility any existing target station or capture region would be too active to handle.

Removing the cooling channel would decrease the capture efficiency from the baseline 0.0672 to 0.0298 good muons per proton, where the latter number includes the effect of adding another chicane. (TODO: 0.0672 number is not final; errors?)

A.3.7 Replacing the target with a horn design

The effect of replacing the solenoidal capture target with a horn was studied in [47]. The main affect was shown to be that only one sign of muon could be captured at any one time. The study showed that the capture efficiency of the horn was between 40 $\%$ and 50 $\%$ compared to the capture efficiency of a solenoid-like target station. It should be noted that the capture efficiency of the Study 2a target station is very similar to the one presented in the RDR.

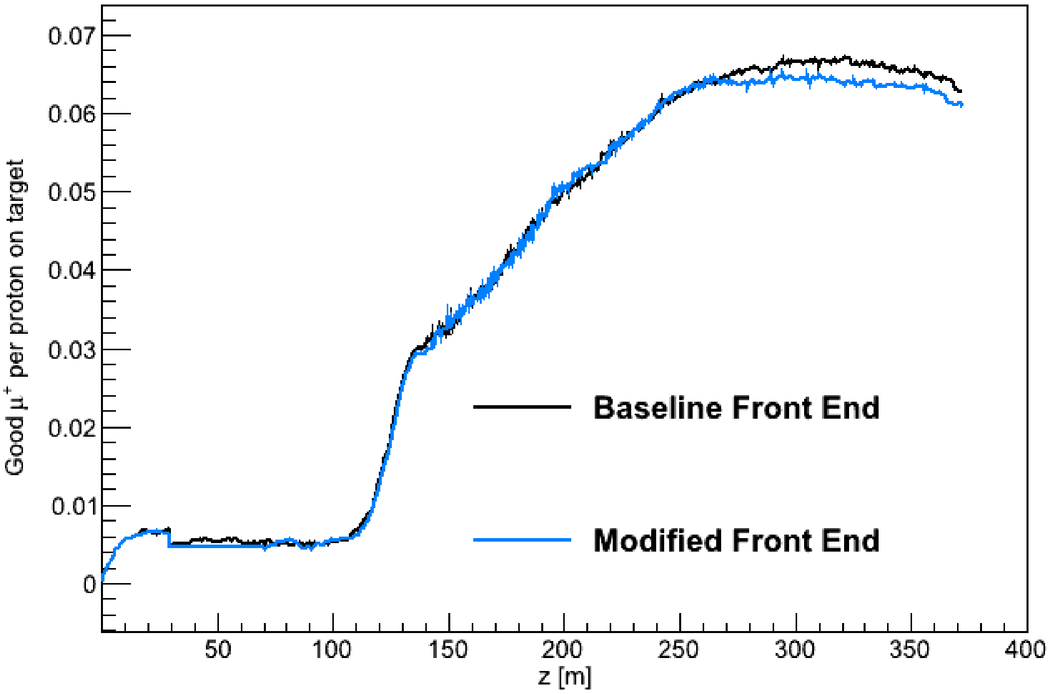

Figure 11: Capture performance of the baseline front end and the modified front end including a long chicane to provide a transverse displacement of the beamline. The cooling channel starts at 129.1 m. Good muons are counted using the standard criterion that muons should be within a momentum band of 100 MeV/c to 300 MeV/c, within a transverse acceptance of 30 mm and a longitudinal acceptance of 150 mm, which corresponds to the acceptance of the acccelerator system.

	Stage 1	Stage 2	Stage 3
700 kW proton driver	0.18	0.18	
CERN 400 kA Horn	0.52		
No cooling channel	0.44		
Total	0.041	0.18	1

Table 3: Fraction of the baseline capture rate that would be achieved by each of the staging options discussed above. The total is found by taking the product of cells in the column above.

A.3.8 Target Geometry Considerations

Despite the introduction of a chicane, the front end beam axis following upgrade would still be 5.4 m from the target station. Some clearance is required for the tunnel in which the front end is expected to sit.

The NuMi/NovA target station has been successfully operated with 400 kW of proton beam power and an upgrade is planned for operation at 700 kW. (TODO: check those numbers) The target station half-width is 3 m. If a similar target station were installed 2.4 m would be available for additional supports and infrastructure associated with a tunnel.

If it were desired to provide a target horn that could operate at 4 MW, additional space may be required. The advantage of operation at 4 MW is that an initial low power proton driver may be replaced by a high power proton driver as an incremental upgrade; followed by a target station and front end upgrade at a later date. Much of the construction work for these upgrades could be performed during operation of the existing facility.

The front end beam pipe in this region is 0.3 m in diameter, with tightly packed RF cavities extending to 0.6 m. In the current design superconducting coils sit outside the RF cavity radius, providing a 1.5 T field. RF power is fed through gaps between adjacent coils. No full magnet design exists but a similar magnet under construction for the MICE experiment has a cryostat outer half width of 1.3 m, leaving 1.1 m for tunnel infrastructure. It may be possible, but would require some care in the design to ensure that the equipment does indeed fit in the tunnel. (TODO: do we want some images here? NOvA? MICE CC? (copyright/authorship issue))

A.3.9 Using a lower powered proton driver

Implicit in the discussion above is the assumption that one may use a lower powered proton driver to feed the target horn. There are several existing facilities that can deliver proton beams of the required beam power, and it is assumed that an existing facility would be used in this case. An additional buncher and bunch compression ring would be required for the protons, as no existing facility has the capability to deliver protons with the required 1-3 ns bunch length.

A.3.10 Rate reduction in proposed staging schemes

The rate of particle interactions in the detector at each stage, as a proportion of the rate for the final stage, is shown in Table 3.

TODO: costing table should be updated with numbers from RDR nf costing - TODO: here I have used scaled costing from euronu with modification to TODO: accomodate lower energy NF

	Stage 1	Stage 2	Stage 3
Proton Driver	6	0	21
Target, capture, decay	8	15	0
Front End	6	12	0
Acceleration	27	0	0
Decay Ring	9	0	0
Detector	13	0	0
Total Cost	65	21	27

Table 4: Cost for the proposed stages, based on [**?**]. Units are cost units [cu], where 1 cu is the cost for 1 % of the euronu acceleratorr facility cost, based on the upper bound estimate for cost.

A.4 Physics Reach of a Staged Facility

The physics reach of the various stages has been examined in detail for configurations with 0.04, 0.25 and 1 times 10^{21} useful muon decays which corresponds to accelerator stage I-III as described in Tab. 4. The detector lends itself well to continious staging, which practically is implied due to the considerable time span required for construction and the fact that a partical detector can be fully operational. A 50 kt partial and a 100 kt full detector are considered. Combined with the three accelerator stages this corresponds to eight luminosity scenarios: 0.02, 0.04, 0.125, 0.25, 0.5, 1. The corresponding physics reach using a 10 GeV muon energy in terms of the accuracy on δ_{CP} is shown in Fig. 12. The two lines labeled 0.02 and 0.04 correspond to the stage I accelerator facility with a 50 kt or 100 kt detector respectively and fall in between the physics reaches of LBNE10 and full LBNE with a 2.3 MW proton driver. This implies that even a minimal stage I facility is competitive to current superbeam experiments. and at the same time provides a clear upgrade path to 5° accuracy without running into systematics issues.

An energy stage at 5 GeV was also investigated and it was found that running at 5 GeV and 2000 km baseline reduces the physics reach by a similar amount as reducing the luminosity by a factor of 2. Combined with the fact that at 5 GeV the acceptance of the 10 GeV storage ring would reduce the actual flux by a factor of ~ 2, makes a 5 GeV energy stage rather unattractive from a physics point of view.

This is to be contrasted with the case where the baseline is changed to 1 300 km and the detector technology is changed as well to a liquid argon detector. In this case it can be shown that the overall sensitivity is quite good because now oscillation maximum, beam flux and detection effeciencies are well matched again. This scenario is studied in detail in the MASS report [48, 49]. On the one hand it demonstrates the flexibility of the neutrino factory concept, on the other hand it makes it obvious that the beam flux, the oscillation maximum and detection efficiencies have to be carefully matched at the beginning. Therefore, neither baseline or energy should be changed as part of a staging scenario; in the initial choice, however, there exists quite some lattitude.

B Conclusion

The feasibility of incrementally developing a 10 GeV Neutrino Factory has been examined and it has been found that the cost and risk can be spread over several stages while delivering competitive physics at each stage and finally enabling a greater degree of precision to be reached.

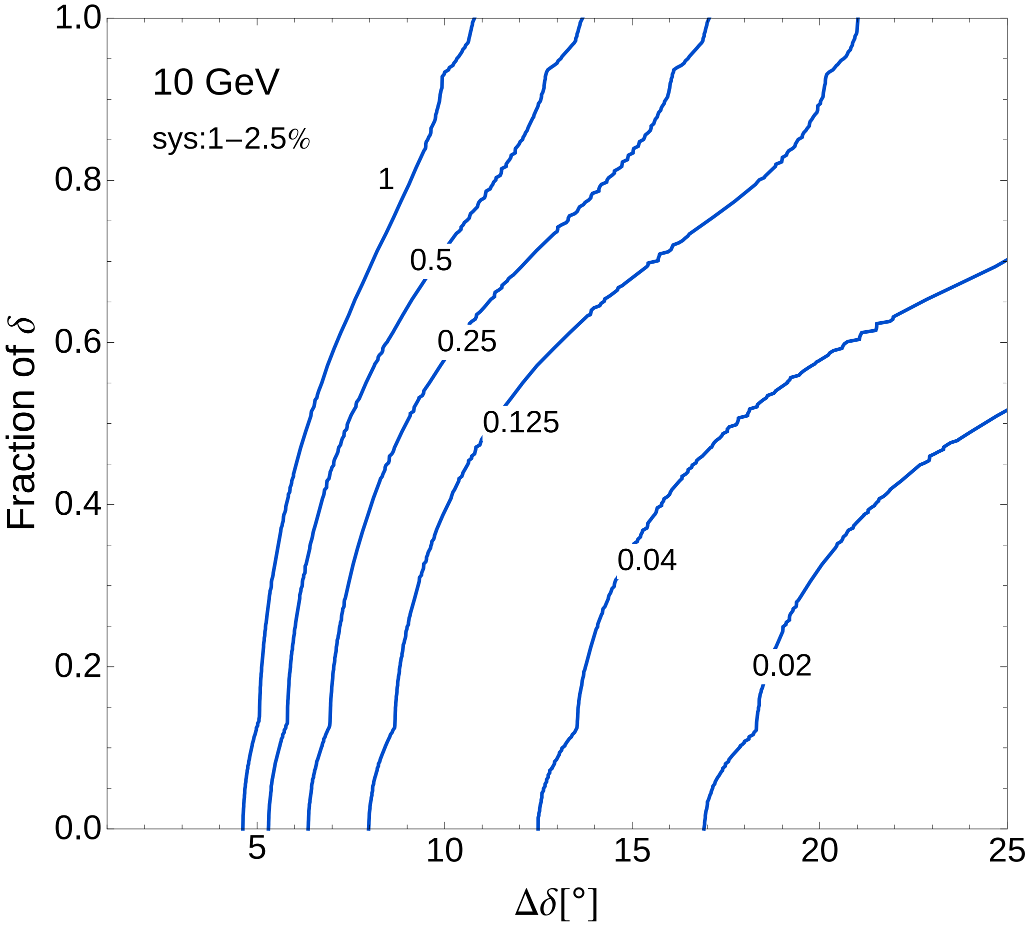

Figure 12: PRELIMINARY – This figure shows the fraction of CP for which a measurement of CP phase δ_{CP} is possible with a certain acccuracy at $1\,\sigma$. The labels correspond the fractional luminosities relative to the full facility, *i.e.* fractions of 10^{21} muons, 100 kt detector and 10 years running time.

C PPEG appendices

Lead author: PH

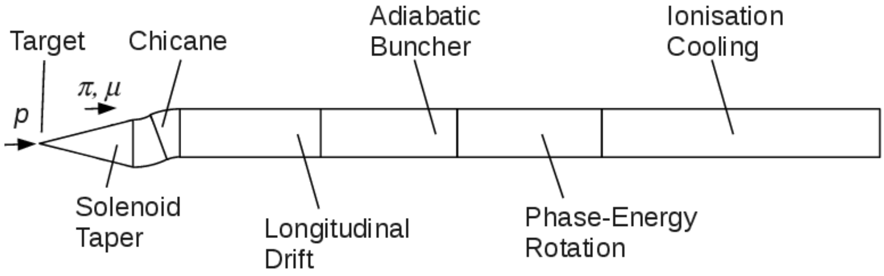

Figure 13: Schematic of the overall front end section.

D The Muon Front End

C. T. Rogers D. Stratakis G. Prior S. Gilardoni D. Neuffer P. Snopok A. Alekou J. Pasternak

The front end is described in outline in Sec. 3.3. In this section some of the details of the lattice simulations are described. Lattice files are available on the launchpad web service [**?**] either by direct download or using the bzr distributed version control system [**?**].

Three simulation codes were used to track the beam in the muon front end. ICOOL version 3.20 [**?**] and G4Beamline version 2.14 (G4BL) [**?**] were used to track the front end, assess capture performance and transmission losses. Initial particle distributions and detailed studies of activation in the decay and chicane region were generated using MARS ¡VERSION¿.

D.1 Decay Region

The target is immersed in a 20 T solenoidal field which tapers to 1.5 T over a distance of about 15 m. In this region, the aperture is considered by the front end group to be a volume of rotation with radius r given by

$$r = \frac{75^2 - 300^2}{15000} z + 75^2 \tag{17}$$

where z is the position along the beamline and units are mm. In G4BL this is modelled as a volume of rotation and in ICOOL a series of cylinders are used with inner edges at 5 mm steps in radius.

Both simulation codes generate fields using infinitely thin current sheets, where an analytical solution exists for the generated fields. In G4BL this is handled automatically by the code, given a certain field tolerance. In ICOOL the sheets are generated manually with 5 sheets generated per coil, with current spread evenly across the coil cross sectional area. The nominal coils used in the simulations are outline in table 5.

A cartoon schematic of the decay region, chicane, proton absorber and longitudinal drift is shown in fig. 14

D.2 Particle Selection System

Protons and particles with momentum above 500 MeV/c are rejected from the front end by means of a solenoidal chicane and Beryllium plug. The chicane filters particles with momentum above 500 MeV/c. The Beryllium plug ranges out low energy protons.

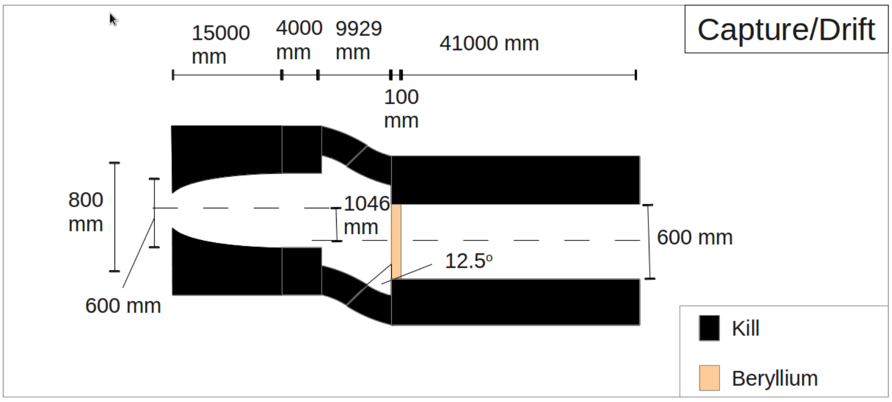

Figure 14: Schematic of the solenoid taper, chicane, proton absorber and drift system.

Coil Number	Front Z	Inner Radius	Outer radius	Length	Current
0	-875.615	183.374	230.974	1001.77	22.0077
1	-1110.25	238.526	287.56	1236.4	20.7391
2	-1209.83	295.812	355.238	2071.54	14.1202
3	-1258.49	362.07	426.417	2120.2	12.0430
4	-1294.60	433.012	501.625	2156.32	10.5919
5	-2409.29	1200	1958.34	3523.19	19.3093
6	1113.91	1200	1843.42	777.842	21.7586
7	2764.71	1200	1958.34	451.954	26.7345
8	4702.37	1199.63	1755.92	312.275	33.4571
9	5757.48	896.518	938.067	2553.68	41.2151
10	9143.17	1182.83	1703.07	154.466	40.7164
11	10347.6	723.607	869.066	129.994	45.0315
12	10850.7	699.214	723.774	3413.12	46.6621
13	14542.8	699.438	863.938	109.612	46.4479

Table 5: Coil pack used for simulation of the solenoid taper.

D.2.1 Chicane and Proton Absorber Conceptual Design

Given that it is challenging to get good muon transmission over the desired range of momenta, and that both positive and negative muon species need to be captured, a stellarator-type solenoidal chicane is proposed. Solenoidal chicanes induce a vertical dispersion in the beam, resulting in symmetric transmission of both particle charges. Matching from the constant solenoid field of the front end to the bent solenoid field is relatively easy. The main problem with this sort of lattice is that it is not possible to make an open midplane solenoid. Either very high radius superconducting coils with significant shielding or normal conducting coils exposed to beam power in the hundred kW range are required. Clearly these components would become active and it is expected that they would be treated as part of the remote handling facility in the target area.

The addition of a Beryllium proton absorber after the chicane serves to lower the overall energy of particles in the system. This stops almost all of the protons, while leaving most muons in the beam. Increasing the absorber thickness and increasing the chicane angle reduce the good muon yield slightly, while producing a dramatic reduction in the proton beam power escaping the system. Based on that, a 12.5° chicane angle and 100 mm proton absorber thickness were chosen. Some details on optimisation of the particle selection system are given in [**?**].

D.2.2 Simulation of the Chicane and Proton Absorber in G4BL

The chicane follows after the solenoid taper region. A 4 m region of matching was used to match from the long coil geometry used in the solenoid taper to a short coil that could be arranged on a torus, all in a 1.5 T field on-axis. In G4BL, a set of match coils provide a match from the long coils used in the solenoid taper to the short coils used in the chicane. Coils in this region are identical with inner radius 430 mm, outer radius 530 mm, length 180 mm and current 16.5703 A/mm^2. A list of current scalings used for matching is given in table 6. Coils are placed with coil centres every 250 mm.

The chicane itself was modelled in G4BL using coils with the same geometry as the match coil, placed every 250 mm along a curved trajectory with radius of curvature of 22.9 m and a total bending angle of 12.5^o. Two bends were placed next to each other, one to provide a positive bending angle and the other to provide a negative bending angle, resulting in a transverse displacement of the downstream linac by 1.0468 m. This suppresses propagation of neutral particles from the target.

D.2.3 Simulation of the Chicane and Proton Absorber in ICOOL

In ICOOL, the solenoid taper field was cut at 15 m and a constant 1.5 T field was used for the following 4 m match. The chicane was modelled using BSOL model 1, which presents a 1.5 T field along the nominal curved trajectory and a $1/r$ dependence off that axis. Two regions were modelled, one with positive radius of curvature and one with negative radius of curvature. No end field was used for the chicane, leading to a discontinuity in field lines at the interfaces between the BSOL regions.

D.3 Chicane Energy Deposition Studies

The initial configuration of the chicane as simulated in MARS15 [50] and shown in fig. 15 starts at the end of the target/capture region, 30 meters downstream from the target, which corresponds to zero in TODO: Check should be 20m Fig. 15. Field maps for MARS simulations were generated by G4BL [**?**]. Coils have inner radius of 43 cm, outer radius of 53 cm, length of 18 cm, with on-axis field of 1.5 T throughout the channel.

Centre Z [mm]	Current Scaling [16.5703 A/mm^2]
15000	0.9
15250	0.8
15500	0.8
15750	0.9
16000	0.95
16250	0.95
16500	0.95
16750	0.95
17000	0.97
17250	0.97
17500	0.97
17750	0.97
18000	1.0
18250	1.0
18500	1.0
18750	1.0

Table 6: Current scalings for the matcher section.

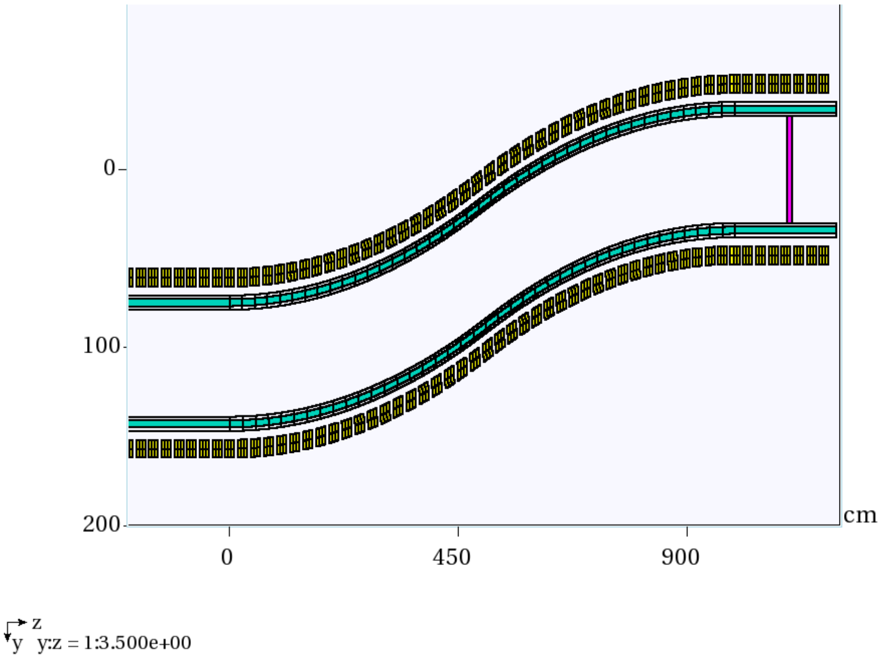

Figure 15: Chicane as simulated in MARS, top view. Yellow: solenoidal coils, cyan: pure W shielding, gray: SS beam pipe and shield pipe around W shield, magenta: 100 mm Be proton absorber.

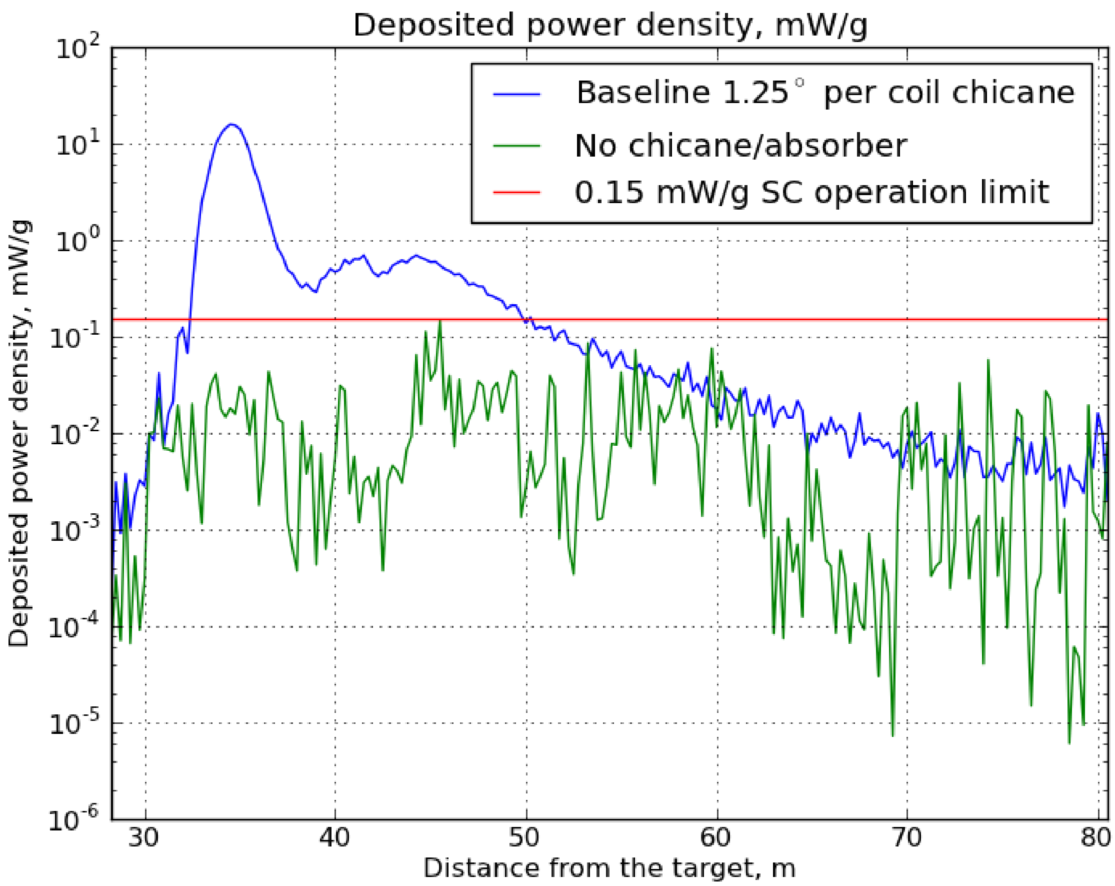

Figure 16: Energy deposition in the coils of the chicane with no shielding, mW/g, nominal 12.5° chicane, used as a reference.

Either copper or a standard MARS material SCON consisting of 90% superconductor (60% Cu and 40% NbTi) and 10% Kapton ($C_{22}H_{10}N_2O_5$) are used for simulations. The proton absorber is a 10 cm Be disk of outer radius 30 cm.

Two conceptual designs for managing the radiation losses in the chicane are available and both are discussed here. The chicane could be implemented using normal conducting copper coils with inorganic insulators to accomodate the significant radiation load. Alternately, the chicane could be implemented using superconducting coils with significant shielding inside the coils.

The case of a chicane without shielding is used as a reference. In this case the peak total deposited power density in the coils is 15.8 mW/g, while a common limit for superconducting coils is 0.15 mW/g. In terms of peak linear power density for the geometry described above that corresponds to 42.6 kW/m for Cu coils, see fig. 16, or 33.3 kW/m for SCON coils. That is significantly larger than the typical 1 W/m limit for hands-on operation. Since these numbers represent averages over the whole coil, a more thorough analysis is required by subdividing the coils into smaller segments in order to localize energy deposition peaks.

D.3.1 MARS simulations, ROOT framework

A recently developed ROOT-based geometry framework for MARS was used for modelling the chicane. The TGeoCtub elementary volume (cut tubes with arbitrary entrance and exit angles) was used to generate segments

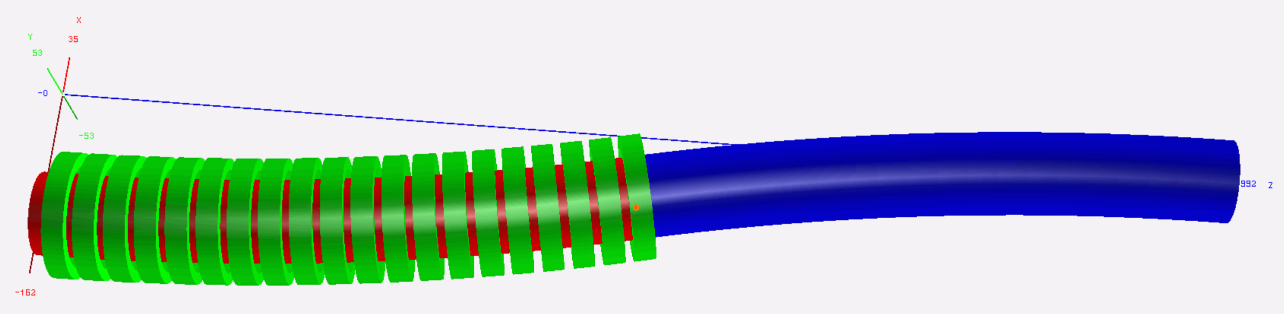

Figure 17: Chicane geometry as defined using ROOT. Red: shield, bend in; blue: shield, bend out; green: half of all the solenoidal coils. Some coils have been removed from the visualisation to display the beam pipe.

of the toroidal beam pipe. The chicane as defined using ROOT is shown in fig. 17.

D.3.2 Coil segmentation

The energy deposition in the chicane is highly asymmetric. Dispersion is excited vertically for particles of intermediate momenta, while high momenta particles are lost transversely on the inside of the bend. Few particles are expected to be lost on the outside of the bend.

In order to correctly account for this effect each coil was represented as a set of segments: 12 azimuthal segments (uniform, 30° each), 2 radial segments, and 3 longitudinal segments, for a total of 72 segments per coil. As expected, even though the average energy deposition per coil is reduced dramatically with the introduction of shielding, there are peaks in the individual segments.

D.3.3 Shielding effect: alternative layouts

The beam pipe in the chicane is wider than in the rest of the front end to permit the dispersion to develop. Two models for beampipe aperture were considered here:

- Bore radius of 42 cm with shielding of radial thickness 35 cm everywhere in the chicane.
- Non-uniform shielding with 30 cm of shielding and bore radius of 30 cm away from the center of the chicane and 40 cm of shielding and bore radius 42 cm around the center of the chicane where the beam is wider.

The chicane layout and the total deposited power density are shown in Fig. 18 for the case of the uniform shielding, and in Fig. 19 for the case of the variable thickness shielding. The density of W is reduced to 60% to account for the tungsten bead packing fraction. The total deposited power density peaks at 1 mW/g for the uniform shielding as represented by the blue line in fig. 20 and at 0.4 mW/g for the non-uniform shielding as represented by the green line in Fig. 20. Where $z \geq 40$ m, electromagnetic showering from the proton absorber produces some energy deposition and additional shielding needs to be considered. The average power density per coil is lower than the 0.15 mW/g limit for the superconducting coils for both cases.

D.3.4 Remaining beam power

The beam power that remains in the beamline downstream of the initial particle selection scheme is shown in fig. 21 for different particle species. The particle selection system is successful at removing the large majority of proton beam power from the beam, although a noticeable fraction of particles do remain.

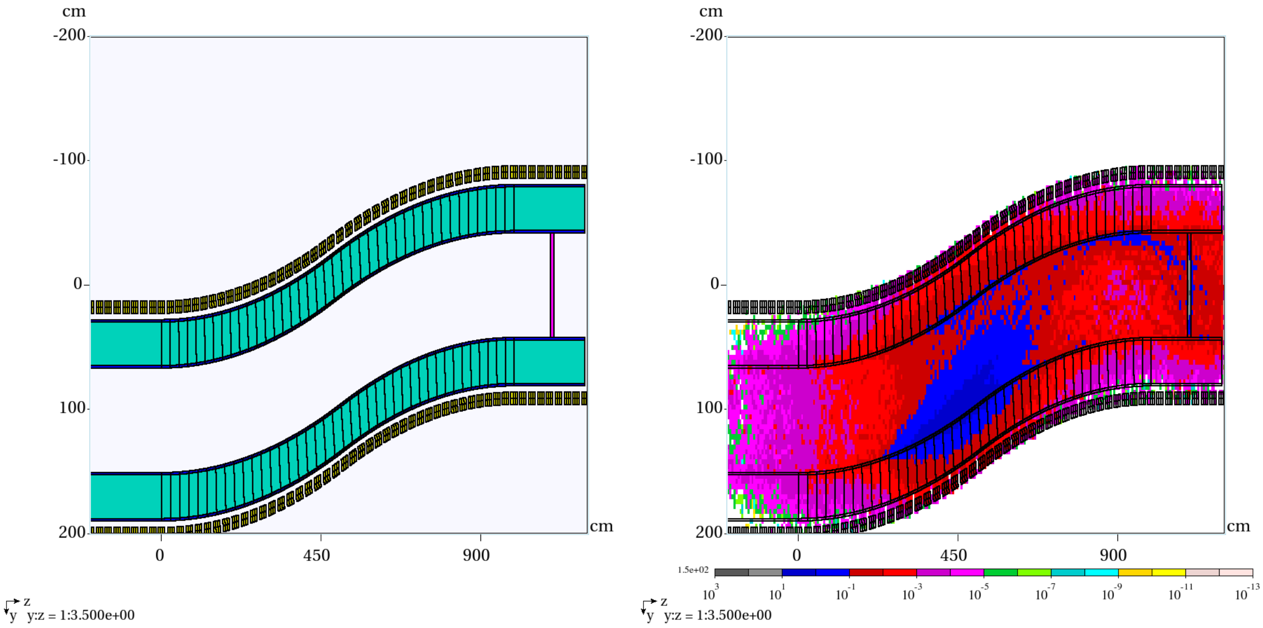

Figure 18: Layout of the chicane with uniform shielding of 35 cm, constant bore radius of 42 cm accommodates beam widening at the center of the chicane. Total power density plot on the right shows that power deposition in the coils is of the order of 0.1 mW/g; however, the quantitative segmented coil analysis shows several peaks larger than the 0.15 mW/g limit.

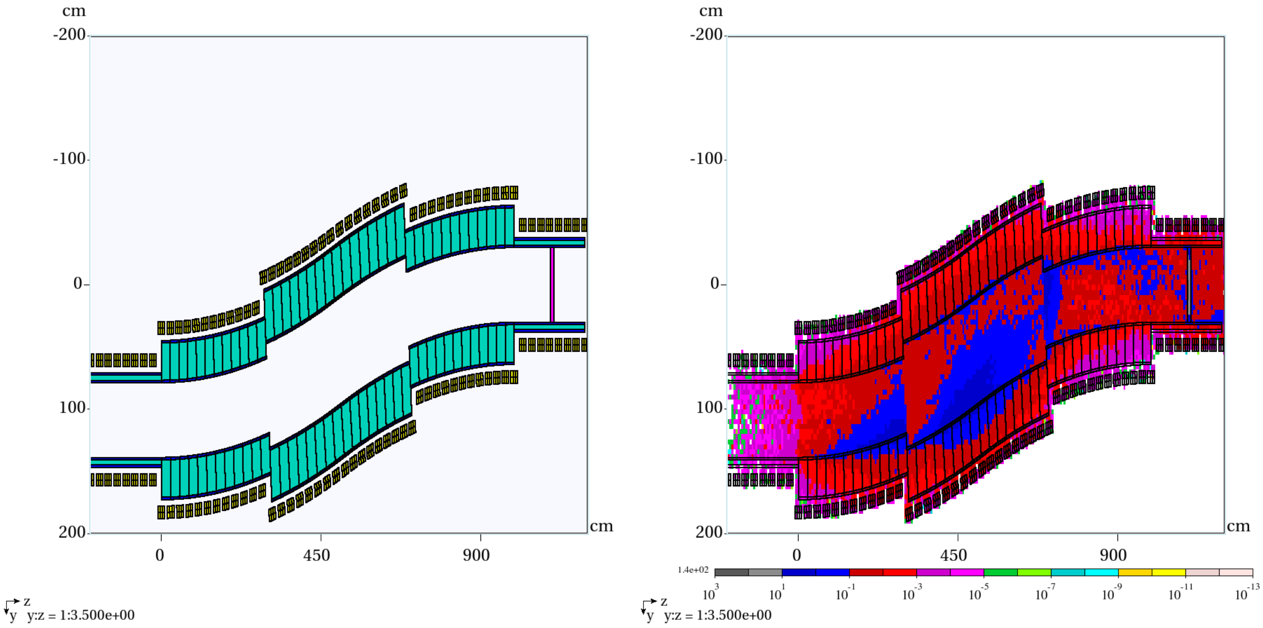

Figure 19: Layout of the chicane with non-uniform shielding of 40 cm around the center of the chicane with a constant bore radius of 42 cm to accommodate beam widening, 30 cm elsewhere in the chicane with a constant bore radius of 30 cm to keep the coil radius smaller. Total power density plot on the right shows that power deposition in the coils within the chicane is of the order of 0.1 mW/g; however, the quantitative segmented coil analysis shows several peaks larger than the 0.15 mW/g limit.

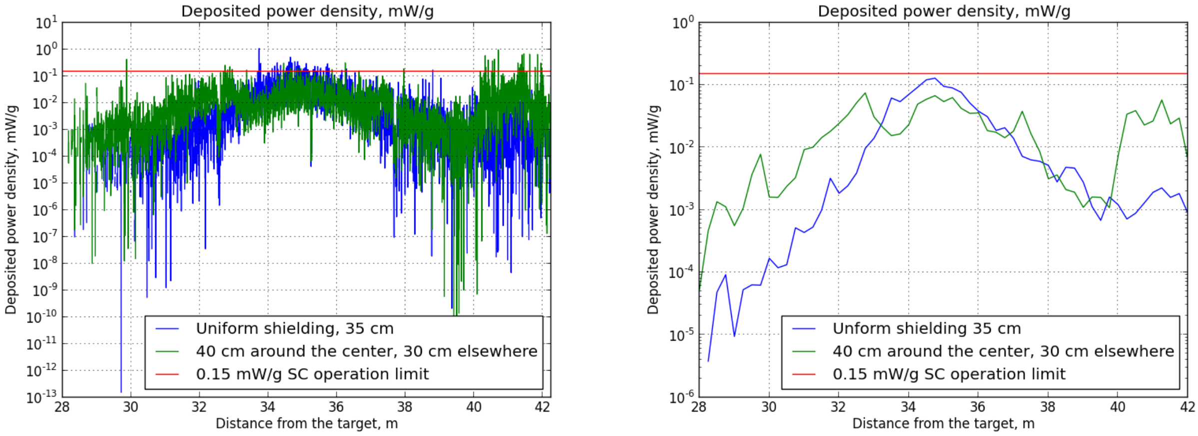

Figure 20: Left: maximum deposited power density for segmented coils, showing a few peaks larger than the 0.15 mW/g limit. Right: average deposited power density per coil is within the 0.15 mW/g limit.

The remaining protons originate from a few high energy particles which seem to scatter through the chicane. The energy distribution of different beam components before the particle selection system, after the particle selection system and at the end of the cooling channel is shown in fig. 22.

D.4 Modifications to the RF capture system

The RF capture system is designed to capture the beam into RF buckets and rotate the longitudinal phase space so that buckets have the same energy. The conceptual design of the system was outlined in [**?**]. Here we describe the parameters of the lattice updated for the modified longitudinal distribution introduced by the particle selection system.

As relevant to the RF capture system, the main effect of the particle selection system is to introduce a mean energy loss of 34 MeV/c for the higher momentum reference particle with initial momentum 270 MeV/c and 41 MeV/c for the lower momentum reference particle with initial momentum 185 MeV/c. This introduces a translation and a slight shear in the longitudinal phase space. A modified capture system is required to capture this distribution efficiently.

Additionally, the position of the RF cavities has been modified to place them every 0.75 m with power feeds envisaged to pass between individual magnet coils.

D.4.1 Longitudinal Drift

In order to bunch and phase rotate the beam, it is necessary to make a longitudinal drift to allow a time-energy correlation to develop. In ICOOL, a constant 1.5 T region with beam pipe radius 0.3 m and length 40.80 metres is used.

A slightly more complicated model is required in G4BL due to the way the geometry is handled. The coil model as outlined in the chicane section is extended for 4.5 m after the end of the chicane. The last 2.5 m of this region is written to a field map file; and then this file is read into G4BL with a scale factor of -1, providing cancellation of the last 2.5 m of field. This creates an abrupt stop to the field map at the nominal end of the particle selection system, some 2 m downstream of the equivalent point in ICOOL. The drift and RF capture can then be simulated using an idealised 1.5 T field.

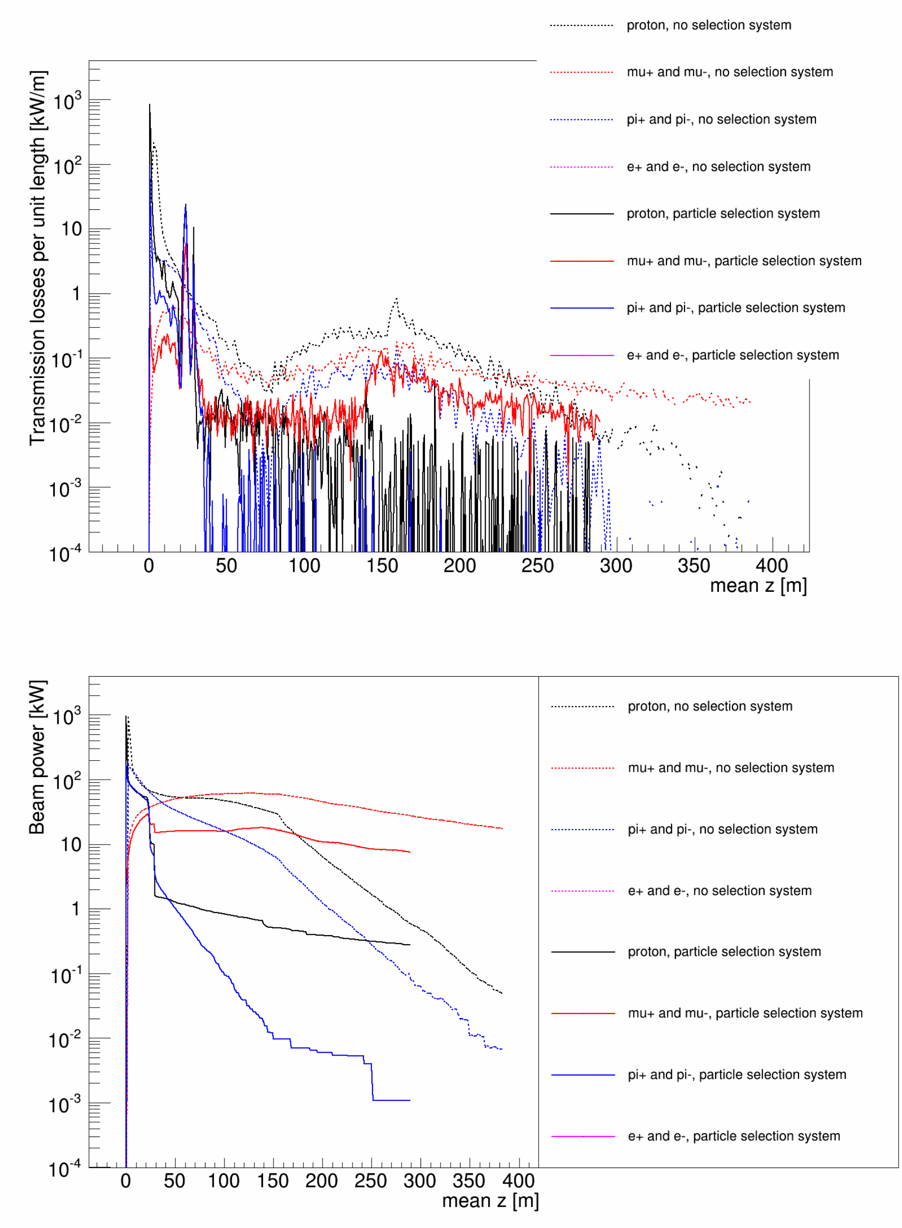

Figure 21: (top) Transmission losses and (bottom) remaining beam power following the particle selection system. Simulation in G4BL 2.14.

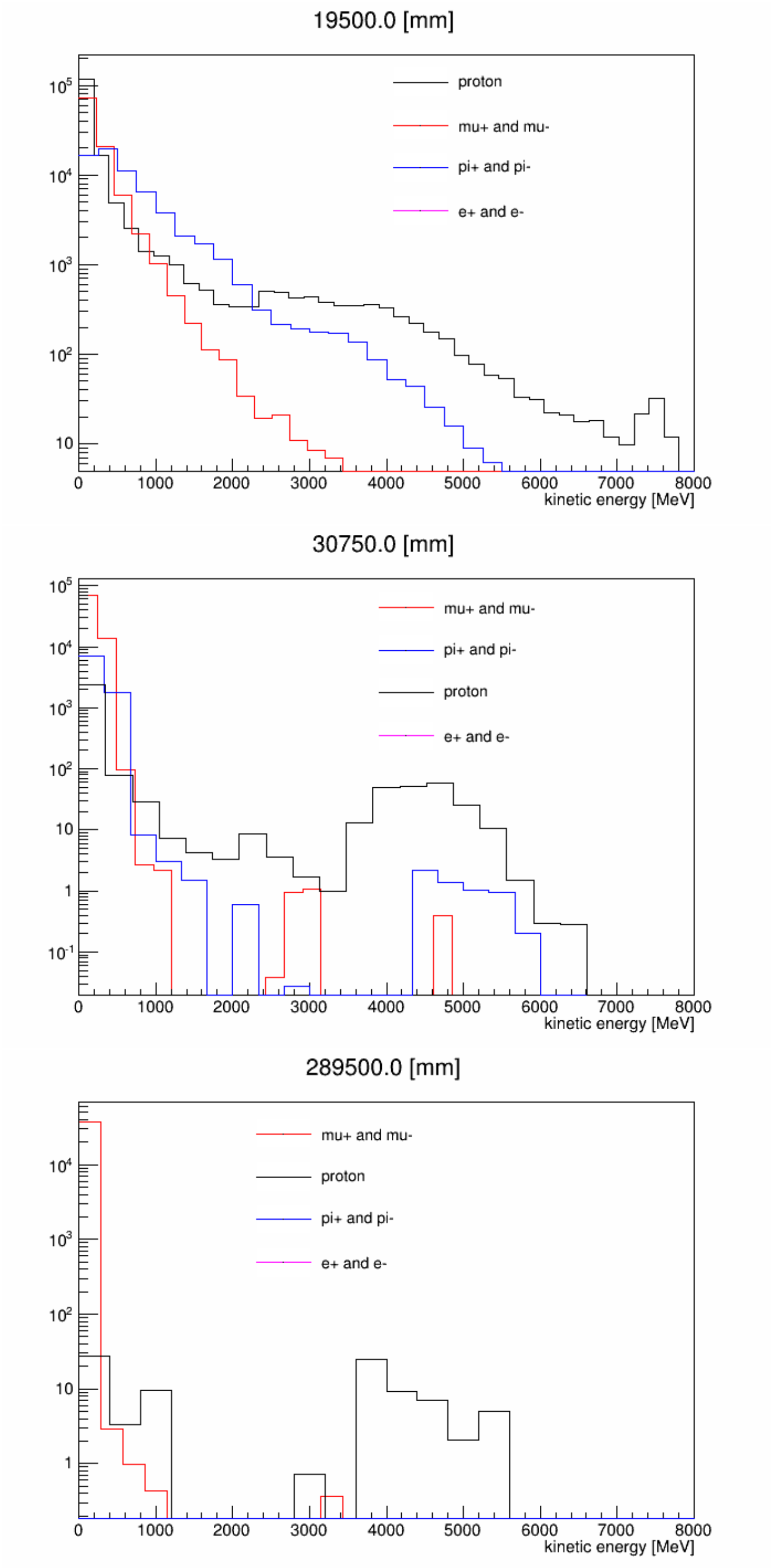

Figure 22: Remaining beam energy, separated by particle type, for position (top) before the particle selection system, (middle) after the particle selection system and (bottom) at the end of the cooling channel. The exact z-position is shown in the plot titles. Simulation in G4BL. 2.14.

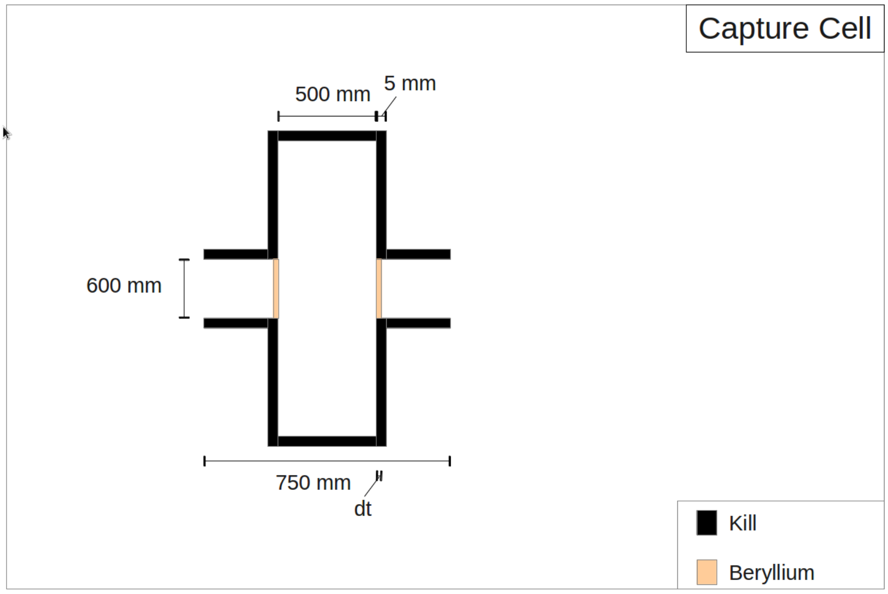

Figure 23: Schematic of a single cell in the RF capture system.

D.4.2 RF capture

The RF capture system frequencies and voltages are outlined below. 0.5 m RF cavities are placed at 0.75 m intervals in a constant 1.5 T field. 200 micron Be windows are placed before and after RF cavities in the buncher. 400 micron Be windows are placed before and after RF cavities in the phase rotator. Windows are intended to enhance the real estate gradient by ensuring higher RF fields are available on the beamline.

TODO: power requirements - calculate by scaling from MICE, assuming same shunt impedance etc but merely changing voltage

D.5 Ionisation Cooling Channel

The ionisation cooling channel design is essentially the same as in the Feasibility Study 2A documentation [**?**]. The cell length has been made longer, to provide space for insulation and support structure for the cooling channel. Additionally, RF and absorbers have been removed from every sixth cell to provide space for bellows.

D.5.1 Matching Section

The magnet section comprises eight 0.75 m long cooling cells that match the beam from the 1.5 T region to the cooling channel proper. Matching for such a high momentum spread is something of an art form, and a precise match is impractical due to significant chromatic and spherical aberrations. No longitudinal match has been attempted.

A schematic of the matching section is shown in fig. 24.

D.5.2 Cooling Section

The cooling section comprises 28 supercells, each of which comprises 5 cooling cells followed by an empty cell to provide space for bellows, diagnostics and other services.

Cell	Frequency [GHz]	Peak Voltage [MV/m]
1	0.35892	0.178
2	0.35892	0.451
3	0.35892	0.724
4	0.35892	0.996
5	0.35892	1.269
6	0.34102	1.542
7	0.34102	1.815
8	0.34102	2.087
9	0.32873	2.36
10	0.32873	2.633
11	0.32873	2.906
12	0.31727	3.178
13	0.31727	3.451
14	0.31727	3.724
15	0.30663	4.269
16	0.30663	4.269
17	0.30663	4.542
18	0.29665	4.815
19	0.29665	5.087
20	0.29665	5.36
21	0.28731	5.633
22	0.28731	5.906
23	0.28731	6.178
24	0.27853	6.451
25	0.27853	6.724
26	0.27853	6.996
27	0.27028	7.269
28	0.27028	7.542
29	0.27028	7.851
30	0.2625	8.087
31	0.2625	8.36
32	0.2625	8.633
33	0.25516	8.906
34	0.25516	9.178
35	0.25516	9.451
36	0.24821	9.724
37	0.24821	9.996
38	0.24821	10.269
39	0.24163	10.542
40	0.24163	10.851
41	0.24163	11.087
42	0.2354	11.36
43	0.2354	11.633
44	0.2354	11.905

Table 7: Design frequencies and peak voltages for the buncher system.

Cell	Frequency [GHz]	Peak Voltage [MV/m]
45	0.23155	13
46	0.23155	13
47	0.22801	13
48	0.22801	13
49	0.22487	13
50	0.22487	13
51	0.22206	13
52	0.22206	13
53	0.2195	13
54	0.2195	13
55	0.21731	13
56	0.21731	13
57	0.21482	13
58	0.21482	13
59	0.21482	13
60	0.21226	13
61	0.21226	13
62	0.21226	13
63	0.2101	13
64	0.2101	13
65	0.2101	13
66	0.20827	13
67	0.20827	13
68	0.20827	13
69	0.20675	13
70	0.20675	13
71	0.20675	13
72	0.20549	13
73	0.20549	13
74	0.20549	13
75	0.20447	13
76	0.20447	13
77	0.20447	13
78	0.20365	13
79	0.20365	13
80	0.20365	13
81	0.20303	13
82	0.20303	13
83	0.20303	13
84	0.20257	13
85	0.20257	13
86	0.20257	13
87	0.20228	13
88	0.20228	13
89	0.20228	13
90	0.20213	13
91	0.20213	13
92	0.20213	13

Table 8: Design frequencies and peak voltages for the phase rotator system.

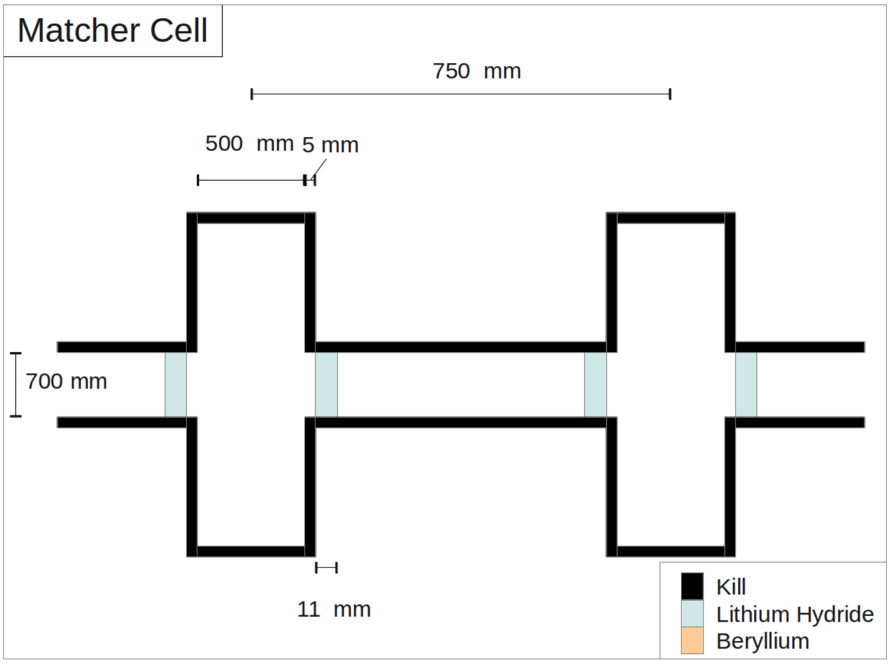

Figure 24: Schematic of a cell in the region between the phase rotation and the cooling proper.

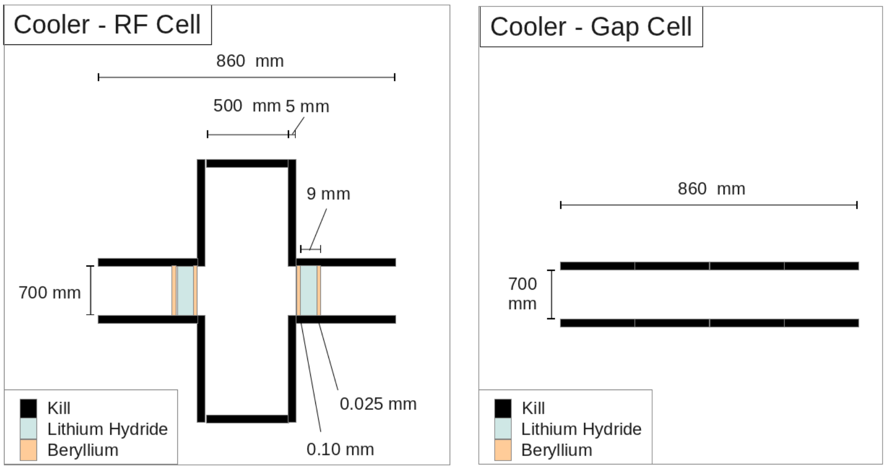

Figure 25: Schematic of a cell in the cooling channel proper.

Coils in this region have inner radius 350 mm, outer radius 500 mm, length 150 mm and current 106.66 A/mm^2. Coils are placed with coil centres every 860 mm, with coils swapping polarity every cell, giving a field of 2.8 T peak on-axis. RF cavities operate with 16 MV/m gradient operating at a nominal 35^o reference phase and are 0.5 m long. Cavity windows are made of Beryllium-coated Lithium Hydride, which absorbs energy to provide ionisation cooling.

D.5.3 Matching from RF capture to cooling

The quality of the transverse match between the RF capture system and the cooling channel can be observed in fig. 26. Some large beta function oscllations and emittance growth can be seen at the interface between the two systems, and this is likely to be due to transverse mismatch in some portion of the phase space occupied by the beam.

Long term beta-beating is observed in the cooling lattice. The origin of the beta-beating is likely to be a longitudinal mismatch which leads to some momentum oscillation within the cooler and a corresponding oscillation in the beta function.

The effect of the longitudinal mismatch on the longitudinal phase space of the beam can be seen in fig. 27. There is a significant longitudinal emittance growth in the beamline. No longitudinal match has been attempted between the cooling channel, and this could likely reduce the emittance growth. There are also significant longitudinal-transverse correlations in the beam that may lead to high transverse amplitude muons becoming dephased from the RF and lost.

D.6 Summary

The Neutrino Factory muon front-end captures a substantial proportion of the muons produced by the Neutrino Factory target. Longitudinal capture is achieved using a buncher and energy-time phase-rotation system while transverse capture is achieved using a high field solenoid adiabatically tapered to 1.5 T and enhanced by ionisation cooling.

Technical risks to the muon front-end are presented by the requirement for high peak RF fields in the presence of intense magnetic fields and irradiation of the accelerator hardware due to uncontrolled particle losses. Strategies have been outlined by which these risks can be mitigated. Overall, the muon front-end increases the capture rate of muons in the nominal accelerator acceptance by a factor 10.

E Front End Engineering

We produced mechanical designs of modules for the bunching, phase rotation, and cooling stages of the front end. All systems consist of RF cavities within a magnetic field. For the buncher and phase rotation sections, that field is a roughly constant 1.5 T, whereas in the cooling the field alternates in sign from one cell to the next. All solenoids are superconducting, while the RF cavities are room temperature with frequencies varying between 201 and 359 MHz. The cavity apertures are closed with beryllium windows are used, similarly to the buncher section, to achieve high gradients. This becomes more challenging as gradients increase in the buncher section, and in the phase rotation and cooling sections, due to the difficulty of removing heat from the windows.

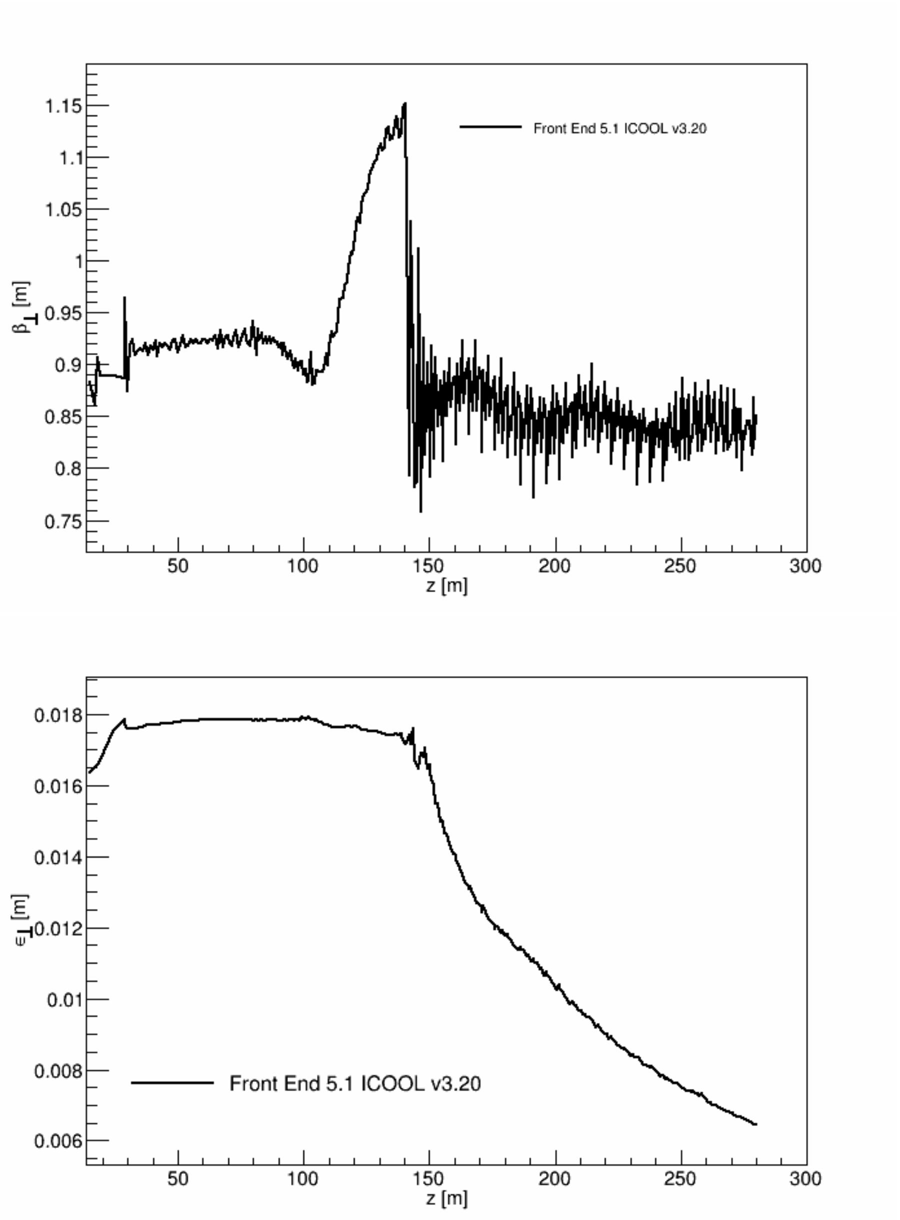

Figure 26: Transverse beam optics following the RF capture system: (top) optical 4D β function [**?**] (bottom) 4D normalised emittance

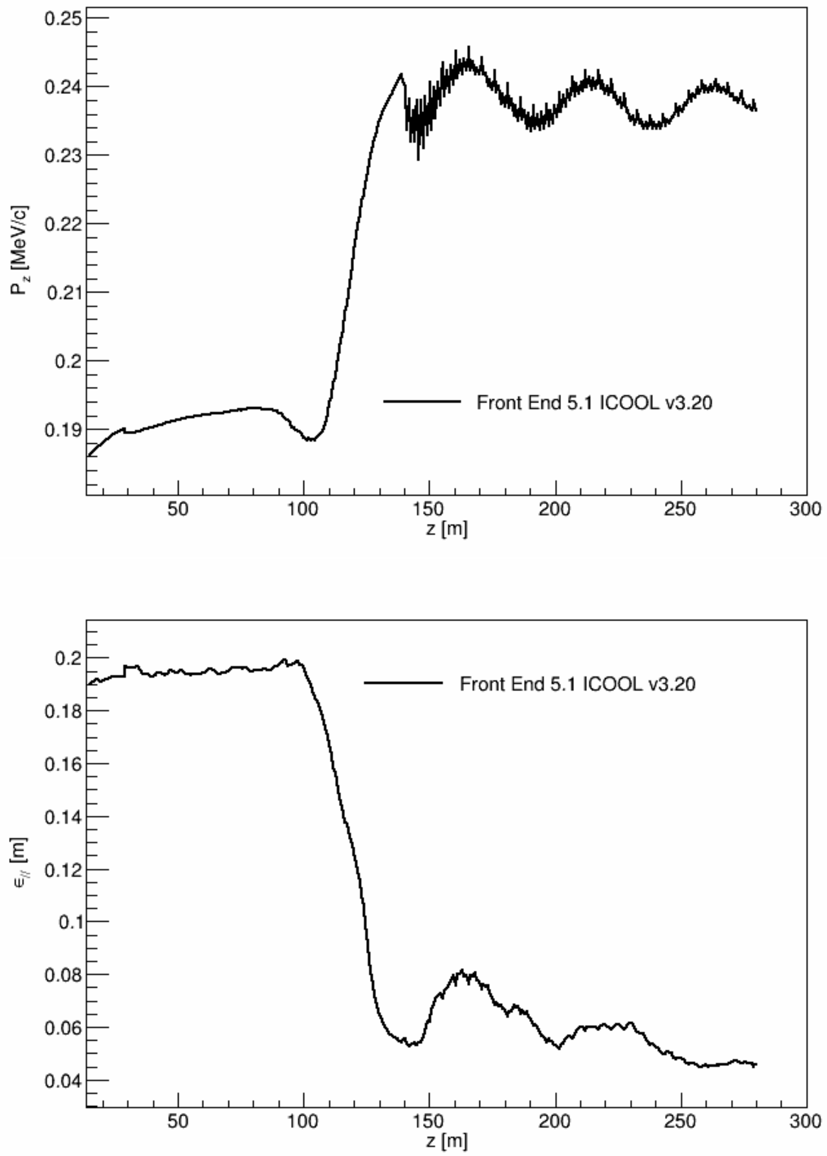

Figure 27: Longitudinal beam parameters following the RF capture system (top) mean longitudinal momentum and (bottom) longitudinal emittance.

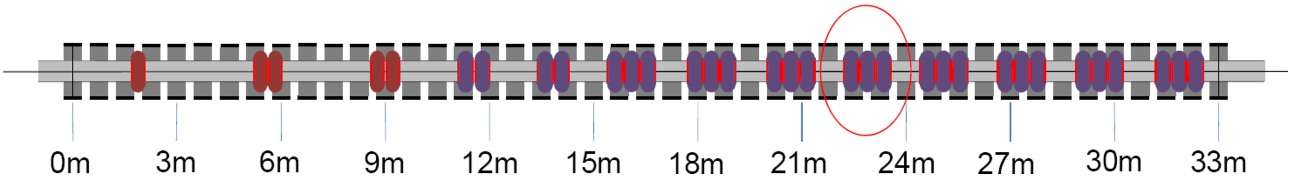

Figure 28: Buncher initial schematic.

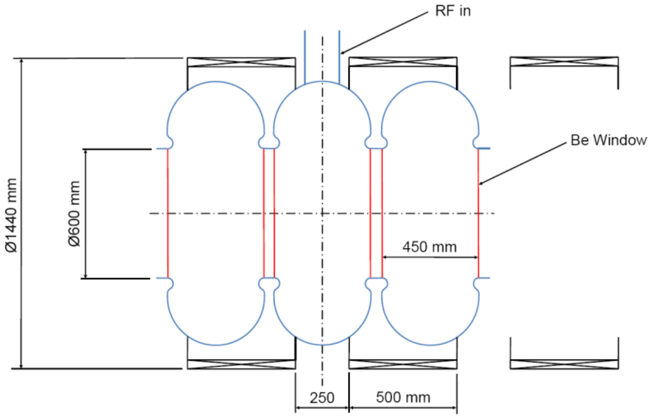

Figure 29: Enlarged illustration of encircled area in Fig. 28.

E.1 Buncher and Phase Rotation

An initial design proposal for an earlier version of the buncher lattice is shown in Fig. 28 with a more detailed depiction of the encircled area in Fig. 29. Due to low gradients required at the beginning of the buncher, fewer cavities with a high gradient were used instead of many cavities with a low gradient. The required voltage increases down the line, and the cavities are grouped into multi-cell modules as this occurs.

The phase rotation has a similar configuration, but due to the consistently high gradient required, an arrangement of cavities and coils shown in Fig. 30 was proposed.

The coil configurations depicted in these figures are in practice not feasible due to the conflicts between the solenoid coils and the RF input coupler. An engineering feasibility study provided a proposal as depicted in Fig. 31. This first iteration modified the schematic to include the RF coupler access to the individual cavities. A bellows was included in every cell to allow cavities to be assembled one-by-one. The design also permits a

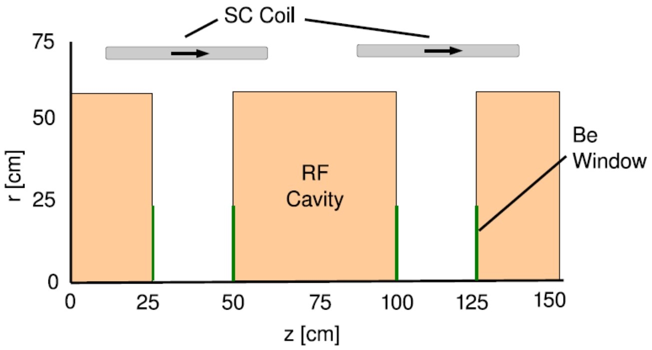

Figure 30: depicting the theoretical layout of the phase rotation module.

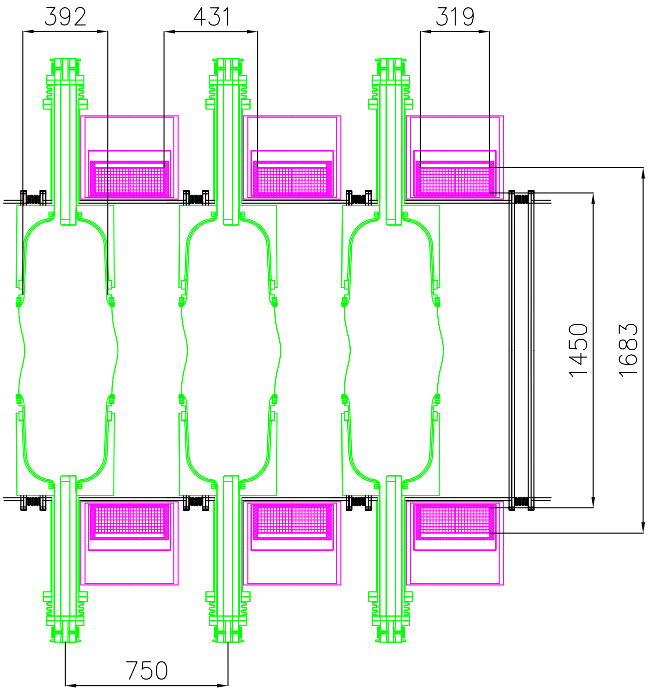

Figure 31: A buncher cell CAD cavity/coil model based on MICE.

Table 9: Solenoid coil parameters for the theoretical lattice design (Original), the engineering design with bellows in every cell (Bellows), and the engineering design with bellows only in cells that are missing cavities (Module). The current density in the original coil was 47.5 A/mm^2.

	Original	Bellows	Module
Length (cm)	50	31.9	50
Inner radius (cm)	68	72.5	72.5
Radial thickness (cm)	4	11.65	11.65

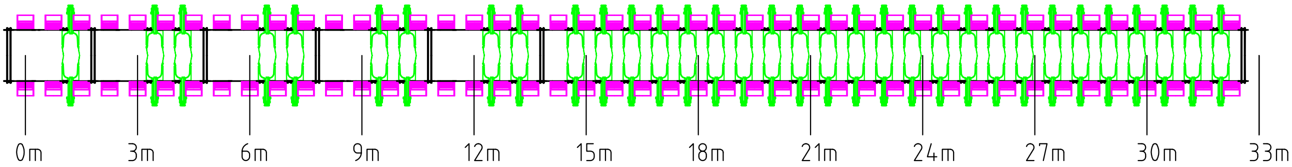

Figure 32: Buncher section with the cell design containing a bellows in each lattice cell.

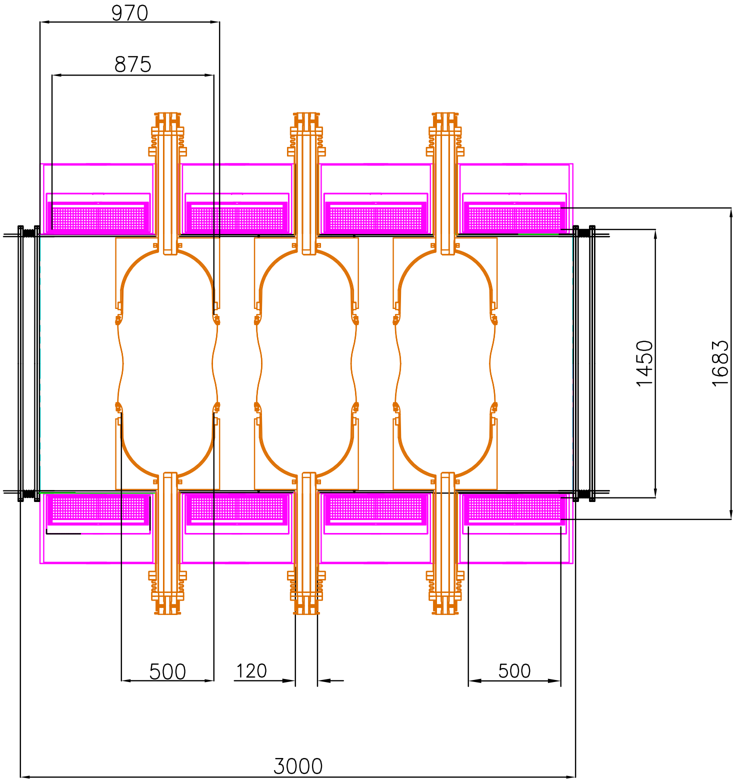

Figure 33: depicting a 3m phase rotation module

lattice cell to lack a cavity (depicted to the right of Fig. 31) so that a module of a group of cavities and coils can be removed without disassembling the entire beam line. The coil geometry for this new configuration is shown in Table 9. The design increases the distance between the coils to accommodate the bellows without changing the 0.75 cm cell length. The buncher lattice in Fig. 28 with these new cells is depicted in Fig. 32. Breaking the design into 3 or 4-cell modules is straightforward at the beginning since there is significant space between cavities at the beginning of the buncher in the earlier design. However, in the latter part of the buncher, splitting into modules becomes more difficult: Figure 32 depicts a large number of cavities in a single module, which may be impractical.

It is preferable to have the cavities grouped into modules, even in the region with higher gradients. Every module can be removed for maintenance or replacement purposes to ensure minimum machine down time. Figure 33 depicts such a module with 4 lattice cells and 4 cavity cells. The disadvantage of this arrangement, in particular for the phase rotation, is that the requirement to periodically remove RF cavities reduces the average RF gradient available. However, raising the 13 MV/m gradient in the phase rotation design to 16 MV/m (the gradient in the cooling), and using modules with 5 lattice cells and 4 cavity cells, gives an essentially identical average RF gradient. The cavity modules can be strung together to increase cost effectiveness further by a common cryogenic feed. A more detailed study will need to be carried out which leads to points being addressed such as additional couplings, enclosure vessels, access areas for instance.

Note that the lattice designs described in appendix BLAH have a constant 1.5 T solenoid field, and have cavities in each cell, even at the beginning of the buncher. Future studies should simulate the design described here to determine the impact of the non-constant solenoid field and the missing cavities on the beam dynamics.

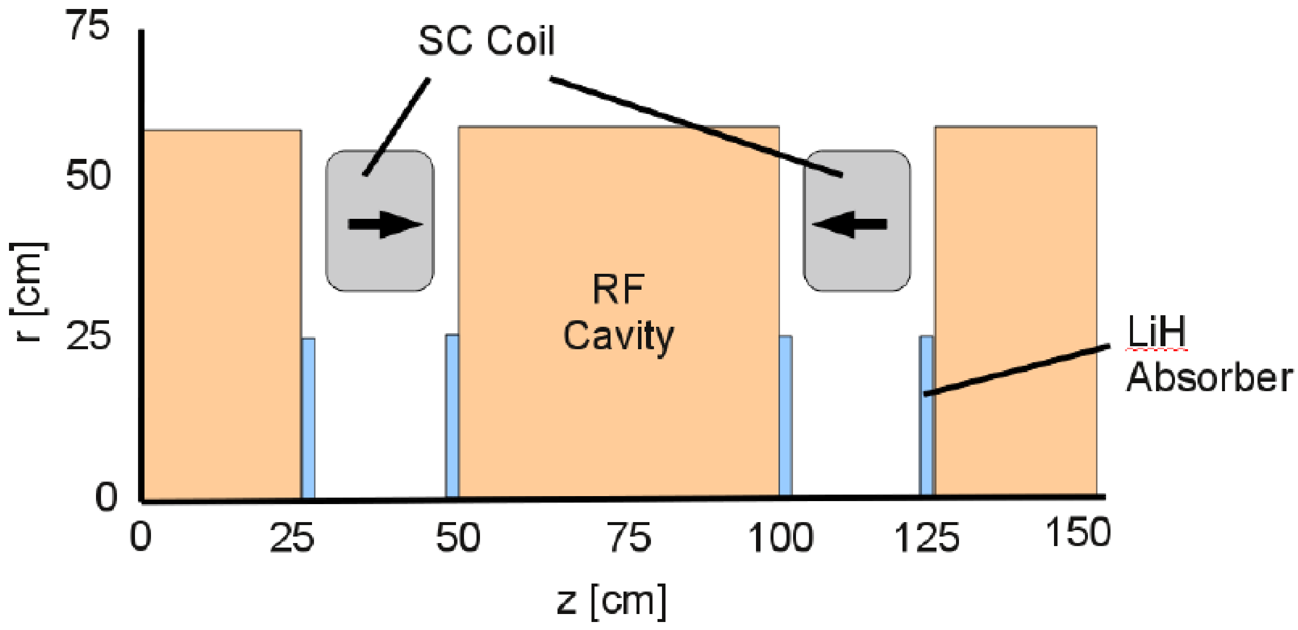

Figure 34: Illustrating the theoretical schematic for a two cell model

Table 10: summary of coil parameters

Length (cm)	15
Inner Radius (cm)	70
Radial thickness (cm)	15
Current Density (A/mm^2)	107

E.2 Cooling

The ionisation cooling channel cells differ from those in the buncher and phase rotator in that the solenoids alternate in sign from one cell to the next, the solenoids have a smaller radius, and the cavities have a LiH absorber at their ends. The cavities are 201 MHz with a gradient of 16 MV/m.

Fig. 34 illustrates the cooling cell layout for the original proposal. This schematic indicates the components required and their relative position. Table 10 gives the solenoid coil parameters.

As for the buncher and phase rotation, the cavities should be grouped into individually-removable modules. We designed such a module, depicted in Fig. 35. The module shown contains 7 coils and 6 cavities is provisionally. From the original specification, the lattice cell increased from 75 cm to 86 cm, but the coil geometry remained the same. The required bellows at the left hand side is the width of one cavity to maintain beam dynamics and provide access to mechanical systems including the vacuum arrangement.

This design is being used in the lattice described in Section XXX, except modules of 6 coils and 5 cavities are used.

The technology and design solution are comparable to the MICE RF Coupling Coil. Fig. 36 demonstrates the size in context. The MICE RFCC module is being built and commissioned at the time of writing.

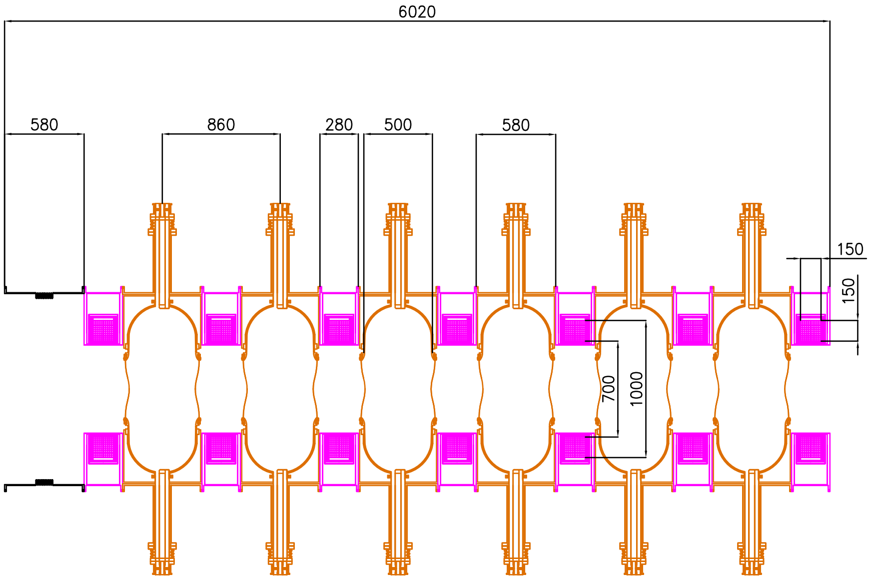

Figure 35: A 6 cavity and 7 coil module. The cavity is 50 cm long. Each solenoid coil cross-section is 15 cm × 15 cm. The cell length is 86 cm instead of 75 cm to accommodate the required vacuum vessels. The vacuum chamber in the empty cell to the left has a bellows at its center.

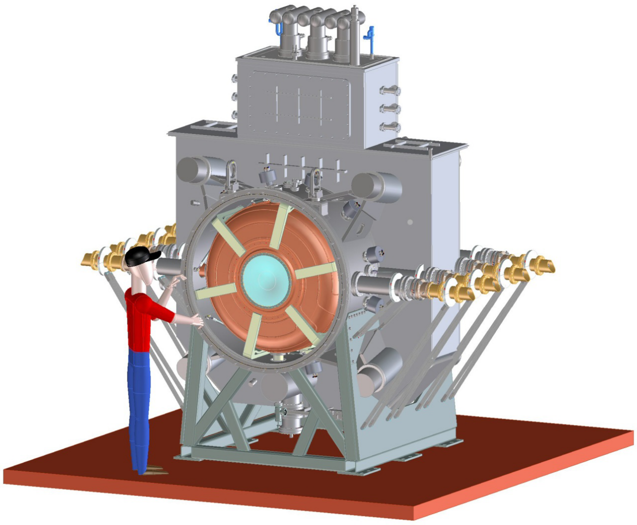

Figure 36: shows a CAD model for the MICE RF Coupling Coil

Figure 37: Pre-LINAC sketch to illustrate the basic layout

Figure 38: depicting a schematic for the 3 m module containing the solenoid (1.5 Tesla) and single cell cavity (201.25 MHz, gain per cavity: 11.17 MeV)

F Acceleration Engineering

Acceleration of the muon beam occurs in a number of stages. The first stage is a pre-linac, which accelerates the beam to 0.8 GeV total energy. This is followed by two recirculating linear accelerators (RLAs), taking the beam to 2.8 GeV and 10.0 GeV, respectively. RLAs are preferable to a series of single-pass linacs since the beam makes multiple passes through the RF cavities (4.5 passes in our design), consequently reducing the cost of the acceleration system. The RLA technique cannot be applied at lower energies, however, since the beam has a low velocity which, combined with its large relative-energy spread and large geometric emittance, would make a linac phased for a higher energy inefficient at the lower, initial energy.

F.1 Pre-LINAC

To increase the energy sufficiently to apply the RLA technique a Linear pre-accelerator raises the total energy from 0.244 GeV to 0.775 GeV. The Pre-LINAC consists of two distinct sections to retain an acceptable beam envelope. See Figure 37 for a sketch of the Pre-LINAC overview. The first part is comprised of a solenoid-single cell cavity module as depicted in Fig. 38 followed by a solenoid-two cell cavity module as shown in Fig. 39.

An initial engineering evaluation led to a reiteration of the design shown in Figures 38 and 39 as the geometry has to be modified to cater for mechanical components such as bellows, vessel enclosures and their interfaces. The challenge of the extremely compact layout coupled with the magnetic shielding requirement requires further investigation. Since solenoids produce strayfields that have adverse effects on the superconducting RF cavities; therefore, a very important design feature of the solenoids is the need to eliminate the strayfields. The solenoids satisfy the following conditions:

1. Are designed to produce zero net magnetic moment. This means that the coil that produces the solenoidal field is bucked by a coil or coils that are larger in diameter.
2. The field from the bucking coils is to be distributed in the same way as the solenoid field. This suggests that the bucking solenoid be around the focusing solenoid so that the return flux from the focusing solenoid is returned between the focusing solenoid and the bucking solenoid.
3. The solenoid pair is surrounded by iron, except where the muon beam passes through it.
4. An iron flux shield is installed between the solenoid magnet package and the RF cavity cells.
5. The superconducting RF cells nearest the focusing solenoid are covered with a type 2 superconducting shield. This will not shield the earth's magnetic field, but it will shield the remaining strayflux from a nearby solenoid.

It can be seen that a distance of 500mm must be maintained in order to negate the effect of the solenoid strayfields on the RF cavity. The physical length of the coils and iron shield had to be reduced by 200mm to

Figure 39: illustrating the initial sketch for the 5 m module containing a solenoid (2 Tesla) and a 2 cell cavity (201.25 MHz, gain per cavity 22.34: MeV):

Figure 40: depicting a more detailed schematic of the solenoid including dimensions (on the left) and magnetic field lines (on the right):

Figure 41: shows the analysis of the magnetic field relative to the cavity longitudinal position.

accommodate mechanical items and provide minimum spacing for vessels for cryogenic purposes. At the same time, the overall length of 3 m could be maintained pending verification by the lattice designer.

A technology solution for the cryogenic requirement is proposed, based on the above parameters and cost constraints. Investigations into cryogenics design lead to the decision to adopt a string cooling approach rather than an individual module for the Pre-LINAC section. A CAD schematic is illustrating this in Fig. B.1.6.

A 2-phase common vessel provides the RF cavity jacket with cooling to 1.8K. This jacket surrounding the cavity is kept to a minimum volume in order to reduce the amount of liquid Helium required. Using a 1.8K temperature alleviates the requirement to invest in exotic materials for the cavities and a Niobium coating suffices to maintain the gradient prerequisite.

Surrounding the 1.8K cavity jacket is a 5K chamber. The solenoid is located in this chamber ensuring it will be superconducting, resulting in the negation of the need to manufacture the coils from Powder In Tube (PIT) or Yttrium Barium Copper Oxide (YBCO) for instance.

The subsequent vessel in turn is a 40K shield acting as the intermediate temperature insulation. The outer structure bringing it to room temperature and may contain a magnet shield if required. It further provides the overall interface bellow between modules.

The input coupler resides within similar insulation layers to prevent its cooling. It further has intercepts at the 5K and 40K shields before passing through the room temperature outer mantle.

This solution applies to the single cell 3m module and the two cell 5m module.

G Decay Ring Lattice Details

G.1 Injection

The six bunches in the ring cross one another alternately at two sets of three crossing points. Injection of each pair of μ^+ and μ^- bunch trains can either be made simultaneously at one of these crossing points or with some delay interleaved between crossing points. The first option is preferred since it allows a longer kicker rise and fall time (Fig. 45) given by

$$\frac{C}{3c} - t_b \tag{18}$$

where C is the ring circumference, c is light speed and t_b is the time duration of a single bunch train. However, simultaneous injection may not be made in the middle of the arc, since muon bunches of each sign would then arrive at the end of a production straight simultaneously. In fact, injection must be at least a distance L_{ex} on either side of the arc centre where L_{ex} is given by

$$L_{ex} = \frac{c}{2}(t_b^{ini} + n_\tau \eta T_0 \delta + t_{gap}) \tag{19}$$

where t_b^{ini} is the initial bunch duration (250 ns), t_{gap} is the desired gap between neutrino signals to be maintained for n_τ mean decay times, δ is the fractional total momentum spread, η is the phase slip and T_0 is the

Figure 42: Placeholder image: Include input coupler detail sketch showing isolation from cryo.

Figure 43: Cryo schematic:

Figure 44: Module interface image (JParc 50 GeV neutrino beamline SC module)

revolution time. Placing an insertion in the production straight is also excluded since it would result in an unacceptable increase in beam divergence. Therefore, the insertion can only be placed between the arc and the matching section to the production straight. To maintain left-right symmetry an insertion must be included at either end of the upper arc. However, insertions are not needed in the lower half of the ring and excluding them helps to increase the production efficiency. Since the insertion contributes to the width of the upper half, the lower arc must be increased in length. To reduce the number of distinct elements in the ring, this is done by increasing the drift lengths while leaving the magnet lengths unchanged.

The zero dispersion insertion is made up of four FDF triplet cells with 3.7 m long drifts in which to place injection magnets. As shown in Fig. 46, a symmetric arrangement of septa and kicker magnets about a central empty drift allows injection of both muon signs from opposing directions. The horizontal phase advance per cell is set close to $\pi/2$ to maximise the displacement at each septum owing to kickers located one and three cells away. The peak fields of both kicker magnets must be equal in magnitude to allow simultaneous injection. Injection settings are listed in Table 12. The injected beam reaches the closed orbit after passing through two opposite polarity kicker magnets. The trajectory of the opposite sign muon bunch will be antisymmetric reflected about the centre of the empty drift. This means that injection will be from the outside of the ring for one muon sign and from the inside of the ring for the other. The available kicker rise/fall time, taking into account debunching up to the point of injection of the final bunch, is approximately 1.37 μs. Apart from the kicker rise/fall time, previous studies indicates that these parameters are realisable [**?**].

A dispersion suppressor section is needed between the arc and the insertion section. The suppression is done by following eleven normal arc cells with three in which the bend angle is reduced by $\frac{2}{3}$. The total number of cells must be increased by two to conserve the total bend (176.4°) in the arc. Note, since the total bend less than π the insertion does not point in the direction of the detectors. Following the dispersion suppressor, an optics matching section comprising four quadrupoles is added. The dispersion suppressor and matching section optics are shown in Fig. 47.

G.2 Overall ring design

Figure 48 shows the lattice functions for the ring.

RF cavity parameters:	3m Module	5m Module
RF frequency (MHz)	201.25	201.25
Aperture Diameter (mm)	460	460
Cells per cavity	1	2
Energy gain/cavity (MeV)	11.2	22.4
Stored energy/cavity (J)	966	1932
Input power/cavity (kW)	490	980
RF on time (ms)	3	3
Loaded Q	106	106

Table 11: Pre-linac RF parameters

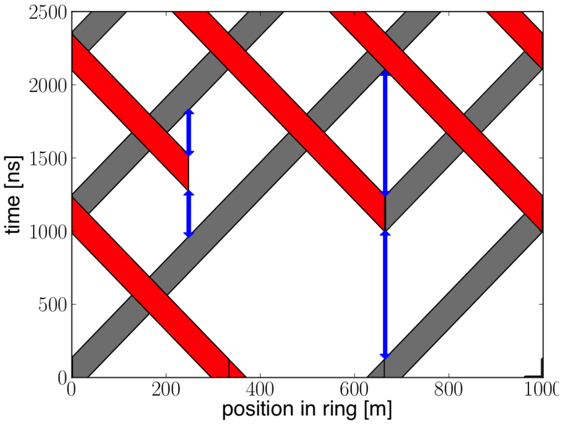

Figure 45: Illustration of the two injection schemes. The grey and red bands represent muon bunches of opposite sign counter-rotating in the ring. The horizontal axis shows the position in the ring with the origin at the end of one of the production straights. The horizontal axis covers the circumference which is arbitrarily chosen. As bunches reach either end of the horizontal range, they wrap around to the other side. The bunch train length is given by the thickness of the band but ignores debunching. The blue arrows on the left and right depict interleaved and simultaneous injection, respectively. The length of the arrows before and after the bunch injection give the available kicker rise and fall time, respectively.

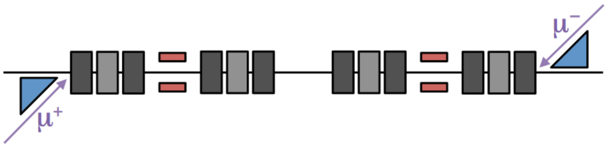

Figure 46: Schematic of the injection insertion showing the septum (blue triangles) and kicker (red squares) magnets.

Tracking studies indicate that the dynamic aperture of the decay ring, assuming no lattice errors, is sufficient to accommodate the required 30πmm acceptance for muons with a momentum spread up to 1%. Above this momentum spread, the dynamic aperture is reduced owing to integer or half integer resonances. The momentum acceptance could be improved by introducing sextupoles to reduce the large chromaticity in the ring (Table 2). The phase space up to the last stable amplitude is shown for on-momentum muons in Fig. 49 and the dependence of dynamic aperture on momentum spread is shown in Fig. 50.

The lattice, subdivided into its main parts (straights, arcs, insertion and matching sections), is described in tables 14–19. Figure 51 shows the beam sizes in the ring, which will determine the required magnet apertures and the pole tip fields in the quadrupoles. Assuming a 30% aperture beyond the beam sizes in Fig. 51, the production straight quadrupoles have an inner radius of 20 cm and pole tips of 0.1 T; for the arc quadrupoles, 8 cm and 1.4 T; and for the insertion quadrupoles 9 cm and 1.1 T.

Table 12: Injection Settings

	Angle (mrad)	**Length (m)**	**Field (T)**	**Rise/Fall Time (μs)**
Septum	67.5	3.0	0.75	-
Kicker	8.1	5.4	0.05	1.37

Table 13: Lattice for straight cell. There are 28 such cells in each of the two straights. The magnet type (superconducting, SC, or normal, NC) is given in the column headed "Type".

Element	**Length** (m)	**Field/Gradient** (T/Tm^{-1})	**Type**
QF	2.0	0.596	NC
Drift	8.0		
QD	2.0	-0.596	NC
Drift	8.0		
Cell length	20.0		
Straight length	562.0		

Table 14: Lattice for one of the fifteen lower arc cells. The magnet type (superconducting, SC, or normal, NC) is given in the column headed "Type".

Element	**Length** (m)	**Field/Gradient** (T/Tm^{-1})	**Type**
QD	0.8	-16.76	SC
Drift	0.395		
Dipole	2.139	-1.6	SC
Drift	0.395		
QF	0.8	17.25	SC
Drift	0.395		
Dipole	2.139	-1.6	SC
Drift	0.395		
Cell length	7.456		
Arc length	112.729		

Table 15: Lattice for the upper arc. There are 11 repeating cells and 3 dispersion suppressor cells (at either end) with one missing and three modified dipoles. The magnet type (superconducting, SC, or normal, NC) is given in the column headed "Type".

Element	**Length** (m)	**Field/Gradient** (T/Tm^{-1})	**Type**
Repeating cell ×11			
QD	0.8	-16.26	SC
Drift	0.3		
Dipole	2.139	-1.6	SC
Drift	0.3		
QF	0.8	16.26	SC
Drift	0.3		
Dipole	2.139	-1.6	SC
Drift	0.3		
Cell length	7.08		
Dipoles in 3 dispersion suppressor cells			
Dipole	2.139	-1.597	SC
Dipole	2.139	-1.6	SC
Dipole	2.139	-0.971	SC
Dipole	2.139	-1.6	SC
Dipole	2.139	-0.632	SC
Arc length	121.16		

Table 16: Lattice for one of the 4 FDF insertion cells. The septum or kicker magnets (defined in Table 12) are located in the long drifts as shown in (Fig. 46. The magnet type (superconducting, SC, or normal, NC) is given in the column headed "Type".

Element	**Length** (m)	**Field/Gradient** (T/Tm^{-1})	**Type**
QF	0.8	12.84	SC
Drift	0.5		
QD	1.6	-11.61	SC
Drift	0.5		
QF	0.8	12.84	SC
Drift	3.7		
Cell length	11.6		
Insertion length	46.4		

Table 17: Lattice for matching section beween end of upper arc and insertion. There are two such matching sections at either end of upper arc. Note the final quadrupole is identical to an insertion QF. The aperture is given by the beam envelope plus 30%. The magnet type (superconducting, SC, or normal, NC) is given in the column headed "Type".

Element	**Length** (m)	**Field/Gradient** (T/Tm^{-1})	**Aperture (m)**	**Type**
Drift	0.51			
QF	0.8	7.55	0.067	SC
Drift	1.92			
QF	0.8	23.903	0.075	SC
Drift	0.568			
QD	0.8	-20.721	0.108	SC
Drift	0.5			
QD	1.6	-1.691	0.101	SC
Drift	0.5			
QF	0.8	12.84		SC
Matching section length	8.793			

Table 18: Lattice for matching section beween the insertion and the production straight. There are two such matching sections on either side of the racetrack. The aperture is given by the beam envelope plus 30%. The magnet type (superconducting, SC, or normal, NC) is given in the column headed "Type".

Element	**Length** (m)	**Field/Gradient** (T/Tm^{-1})	**Aperture (m)**	**Type**
Drift	0.5			
Dipole	2.0	-1.063	0.067	SC
Drift	1.5			
QF	0.4	20.935	0.073	SC
Drift	2.1			
Dipole	2.0	0.860	0.171	SC
Drift	3.5			
QD	0.4	-8.524	0.258	SC
Drift	1.2			
QD	0.8	-6.391	0.256	SC
Drift	1.2			
QF	0.4	16.895	0.19	SC
Drift	1.2			
Dipole	2.0	-0.320	0.189	SC
Drift	1.2			
Matching section length	20.4			

Table 19: Lattice for matching section beween lower arc and the production straight. There are two such matching sections on either side of the racetrack. The aperture is given by the beam envelope plus 30%. The magnet type (superconducting, SC, or normal, NC) is given in the column headed "Type".

Element	**Length** (m)	**Field/Gradient** (T/Tm^{-1})	**Aperture (m)**	**Type**
Drift	0.9			
Dipole	2.0	0.591	0.077	SC
Drift	1.5			
QF	0.4	14.231	0.106	SC
Drift	5.0			
Dipole	2.0	-0.645	0.159	SC
Drift	3.5			
QD	0.4	-6.555	0.230	SC
Drift	1.1			
QD	0.8	-5.729	0.231	SC
Drift	1.1			
QF	0.4	12.186	0.187	SC
Drift	1.1			
Dipole	2.0	-0.468	0.189	SC
Drift	1.1			
Matching section length	23.3			

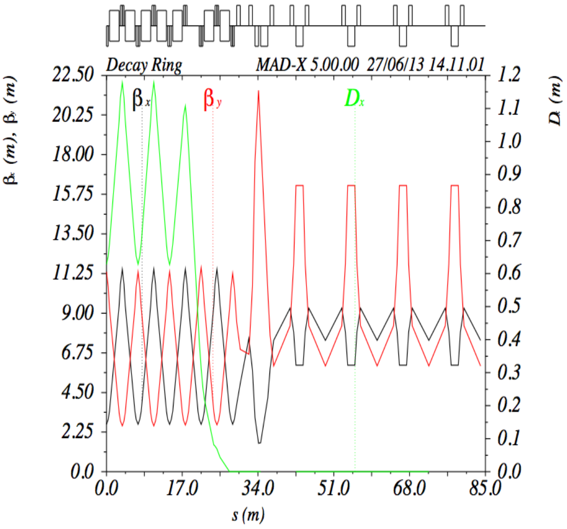

Figure 47: Matching from arc to insertion calculated using MAD-X[51].

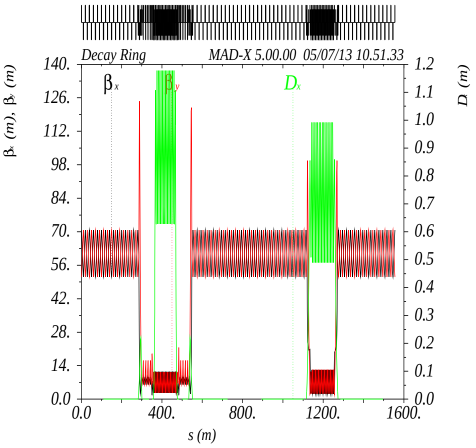

Figure 48: Decay ring optics. The origin corresponds to the middle of a production straight and the optics of the upper part of the ring are shown on the left.

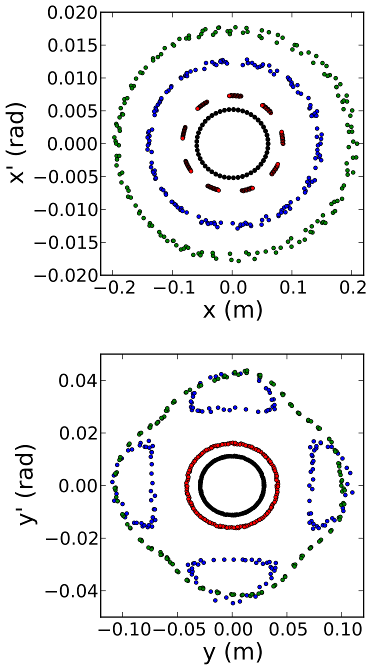

Figure 49: Phase space plots in the horizontal (top) and vertical (bottom) planes up to the maximum stable amplitude in an ideal lattice assuming zero momentum spread. Single particles were tracked for four mean decay times. The innermost black points show the required 30π mm acceptance. The other amplitudes, shown in red, blue and green, are 60π mm, 180π mm and 360π mm, respectively.

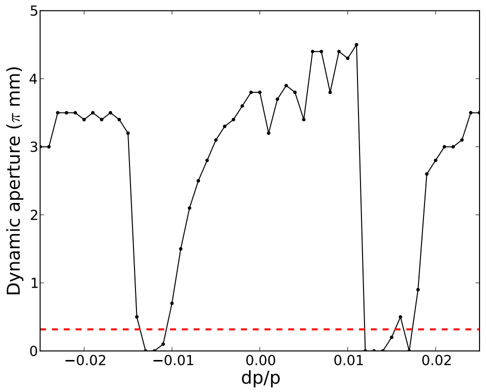

Figure 50: Dynamic aperture for off-momentum particles. The horizontal line shows the required acceptance.

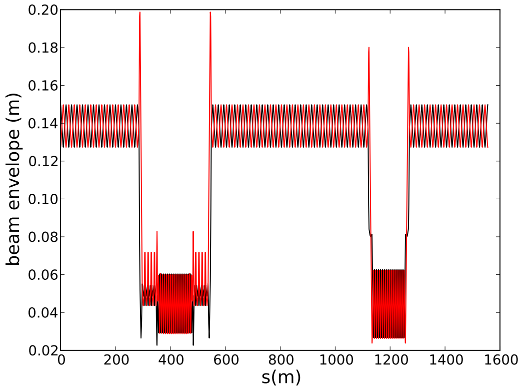

Figure 51: Full beam sizes in the ring.

H Detector working group appendices

Lead authors: PS, ABr, JM, RT

I Cost estimate

Lead authors: JPa, AK